

1-2018

Carbon Nanotube Ultracapacitor Characteristics and Cell Design

Antonis A. Orphanou

Santa Clara University, aorphanou@scu.edu

Follow this and additional works at: https://scholarcommons.scu.edu/eng_phd_theses



Part of the [Electrical and Computer Engineering Commons](#)

Recommended Citation

Orphanou, Antonis A., "Carbon Nanotube Ultracapacitor Characteristics and Cell Design" (2018). *Engineering Ph.D. Theses*. 12.
https://scholarcommons.scu.edu/eng_phd_theses/12

This Dissertation is brought to you for free and open access by the Student Scholarship at Scholar Commons. It has been accepted for inclusion in Engineering Ph.D. Theses by an authorized administrator of Scholar Commons. For more information, please contact rscroggin@scu.edu.

SANTA CLARA UNIVERSITY
Department of Electrical Engineering

I HEREBY RECOMMEND THAT THE DISSERTATION PREPARED UNDER MY
SUPERVISION BY

Antonis A. Orphanou

TITLED

Carbon Nanotube Ultracapacitor Characteristics and Cell Design

BE ACCEPTED IN PARTIAL FULFILLMENT OF THE REQUIREMENTS FOR THE DEGREE

OF

DOCTOR OF PHILOSOPHY IN ELECTRICAL ENGINEERING



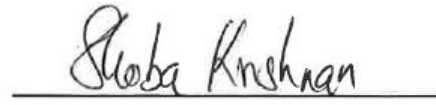
CARY Y. YANG (ADVISOR)



TOSHISHIGE YAMADA



DRAZEN FABRIS



SHOBA KRISHNAN



NOBUHIKO KOBAYASHI



STEPHEN HUDGENS

January 18, 2017

**CARBON NANOTUBE ULTRACAPACITOR
CHARACTERISTICS AND CELL DESIGN**

ANTONIS AVGOUSTINOS ORPHANOU

B.S. UNIVERSITY OF ARIZONA, 1992

M.S. UNIVERSITY OF ARIZONA, 1996

A DISSERTATION SUBMITTED IN PARTIAL FULFILLMENT OF
THE REQUIREMENTS FOR THE DEGREE OF DOCTOR OF
PHILOSOPHY IN ELECTRICAL ENGINEERING

SCHOOL OF ENGINEERING

SANTA CLARA UNIVERSITY

SANTA CLARA, CALIFORNIA

JANUARY, 2017

Acknowledgements

I would like to take this opportunity to express my deepest gratitude and appreciation to Santa Clara University and the faculty whom I have crossed paths with, for giving me the opportunity and excellent guidance to pursue my academic dream.

I would like to express my sincere gratitude and deepest appreciation to my advisor, Prof. Cary Yang, who has guided, supported, and mentored me throughout my doctoral program. I would like to thank him for giving me the opportunity to be part of his TENT research group at Santa Clara. His patience dealing with a full-time working engineer and part-time student is deeply appreciated.

I would also like to express my gratitude to Prof. Shoba Krishnan, Prof. Drazen Fabris, and Prof. Nobby Kobayashi for being part of my Ph.D. Committee. I thank them for their advice and challenging comments and suggestions, which were critical to the continuous improvement of my research effort.

Lastly, I would like to express my deepest gratitude to Prof. Toshishige Yamada. This research project was exclusively his idea at the outset. His technical genius, guidance, and mentoring throughout my doctoral research made the completion of this work possible.

Abstract

A model of carbon nanotube (CNT) ultracapacitor (CNU) as a high-performance energy storage device is developed based on simulations of electrolyte ion motions between cathode and anode. Using a molecular dynamics (MD) approach, the equilibrium positions of electrode charges interacting through Coulomb potential are determined, which in turn yield the equipotential surface and electric field associated with the capacitor. With an applied AC voltage, the current is computed from the nanotube and electrolyte particle distribution and interaction, resulting in a frequency-dependent CNU impedance. From the current and impedance profiles, the Nyquist and Cyclic Voltammetry plots are then extracted. Results of these calculations compare well with existing experimental data. A lumped-element equivalent circuit for the CNU is proposed and the impedance computed from this circuit correlates well with the simulated and measured impedances.

Further, a methodology is developed to optimize vertically grown carbon nanotube CNU geometrical features such as CNT length, electrode-to-electrode separation, and CNT packing density. The electric field and electrolyte ionic motion within the CNU are critical in determining device performance. Using a particle-based model (PBM) based on MD techniques, developed for this purpose, the electric field in the device is computed, the electrolyte ionic motion in the device volume is tracked, and the CNU electrical performance as a function of the aforementioned geometrical features is determined. Interestingly, the PBM predicts an optimal CNT packing density for the UC electrodes. Electrolyte ionic trapping occurs in the high CNT

density regime, which limits the electrolyte ions from forming a double layer capacitance. In this regime, the CNU capacitance does not increase with the CNT packing density as expected, but decreases significantly. The results compare well with existing experimental data and the PBM methodology can be applied to an ultracapacitor built from any metallic electrode materials, as well as vertically aligned CNTs studied here.

Contents

1. Introduction.....	1
2. Simulation Methodology and Theoretical Background.....	8
2.1 Defining simulation cell and scaling considerations.....	9
2.2 Coulomb interactions, boundary conditions and conservation of energy in the unit cell.....	11
2.3 Particle dynamics in unit cell.....	14
2.4 Boundary conditions in unit cell.....	16
2.5 Total current in simulation unit cell.....	18
2.6 Derivation of scaling relationships between simulated and real CNU Cell.....	21
2.6.1 Velocity preservation.....	22
2.6.2 Electrolyte collision period and resistance preservation.....	22
2.6.3 Time and frequency scaling.....	23
3. Simulation of CNU Using Molecular Dynamics.....	25
3.1 Nyquist plot extraction and comparison to experiment.....	26
3.2 CV plot extraction and comparison to experiment.....	28
3.3 Simulation of electrolyte ionic polarization.....	29
3.4 CNU equivalent circuit.....	32
4. Design Criteria for CNU Cell.....	35
4.1 Cell design considerations.....	35
4.2 Electrode-Electrode separation.....	37
4.3 CNT length.....	38
4.4 CV scan rate, simulation versus experiment.....	39
4.5 Effect of CNT density on CNU performance and ionic traps.....	41
5. Conclusions and Future Work.....	50
6. Appendix A. Computational Algorithm Flow Diagrams.....	56

Chapter 1

Introduction

The study of ultracapacitors (UC) or supercapacitors has been the subject of intense research in recent years [1-3]. Increasing the total capacitor electrode surface area S to maximize the device stored energy has always been a prohibitive challenge. The use of nanomaterials as capacitor electrodes has been studied recently [4-14], as many of these materials are low-dimensional with high surface area to volume ratio and, when properly integrated onto a metallic electrode substrate, S increases significantly. Such low-dimensional nanomaterials can be metallic or semiconducting, just like their macroscopic counterparts, with some notable exceptions. For example, silicon chains are not semiconducting but generally metallic. Thus careful examination of the suitability of materials to serve as capacitor electrodes is required [15-17]. Graphite (3-D) is metallic, and so is graphene (2-D), but carbon nano-tubes (CNTs) (1-D) can be either metallic or semiconducting [18]. When semiconducting nanotubes are contacted to metal electrodes, Schottky or tunneling barriers can be created [19-22] and achieving low-resistance ohmic contact is a major challenge. Nevertheless, there are many studies on UCs using nanocarbons [4, 5, 22], as their chemically inert surfaces do not require electrode passivation layers. Initially, UCs were made of porous carbons [6]. Subsequently, activated carbons [7], nanotubular materials [8], CNTs [9], carbon aerogel composites [10], fibrous carbon [11], carbon/graphene nanotube composites [12], and graphene [13] were investigated as alternative electrode materials. Most UCs contain an electrolyte since capacitance significantly increases with its inclusion, due to the formation of a double layer capacitance (DLC), which is the capacitance between the electrolyte ions and the electrode charges separated by nanoscale

distances [14, 23-27]. DLC formation can also be interpreted as an effect of screening by electrolyte ions from electrode charges, since if such charges are perfectly screened, the electric field in the capacitor volume is zero.

Capacitor performance is often evaluated with a Ragone plot of energy density versus power density [28]. Conventional capacitors generally possess power densities higher than 10^4 W/kg, but a low energy density typically in the 0.01~0.05 Wh/kg range, making it unsuitable for high-performance energy storage applications [29-32]. It was recently reported [13] that by using graphene to increase S , UCs can yield as much as 86 Wh/kg, thus demonstrating significant potential for nanocarbon UCs. Vertically aligned or randomly oriented CNT arrays or graphene sheets have been shown to increase S and the capacitor energy storage capacity drastically [30-32].

To achieve a large S , an array of vertically aligned CNTs can be grown on a metal surface with a high areal density, forming a highly conducting electrode [33]. Thus, CNTs are chosen as the electrode material for our study of UC. In particular, single-walled carbon nanotubes (SWNTs) have a specific capacitance of 180 F/g, compared to the specific capacitances of activated carbon and aerogels, 100 F/g and 104 F/g, respectively. We model the CNTs as solid conductive structures protruding from the capacitor electrode plate at a given density. Our model is two-dimensional and in a three-dimensional equivalent, the cylindrical CNT is approximated by a rectangular block. Thus, linear rather than areal density is used. Our model does not describe the breakdown of the DLC by the electrolyte solvent and hence pseudo-capacitance (due to charge transfer between electrolyte and electrode) is neglected. This point is elaborated further in the discussion on extraction of the Cyclic Voltammetry plots in Chapter 3.

The CNT corrugations in the electrode are so dense and electrically singular that the electric field and electrolyte ion spatial distribution within the device cannot be assumed uniform or symmetric in response to an electrical signal. In other words, the DLC would not be formed uniformly along the electrodes due to the abrupt and dense CNT corrugations. This is in sharp contrast to traditional commercial UCs, in which the corrugations are smooth, shorter in length, and not as dense. One of the well accepted models, proposed by de Levie [34], is an analytical equivalent-circuit-based compact model, most suited for the analysis of these commercial UCs with smooth corrugations. Under the de Levie model assumptions, due to the “smooth” nature of the electrode, the DLC is uniformly and symmetrically formed following the contour of the electrode surfaces. Under these conditions, it is reasonable to assume the electrolyte as a homogeneous neutral jellium, suitable for invoking the de Levie model. However, in many nanomaterial-based UCs, changes in corrugations are abrupt and significant. Therefore, we can no longer assume that the electrolyte is spatially uniform or the electric field is uniform along the electrodes or within the capacitor. Thus, the formation of the DLC will have to be re-examined using a new approach that can potentially resolve the existing model limitations, as described above. This is critical in understanding UC response to an AC voltage input, which is known as the device Nyquist characteristics [1]. We examine these electrode non-uniformities in detail using examples of CNUs where long and dense CNT arrays protrude from conducting surfaces. For such a study, it is not appropriate to use the homogeneous neutral jellium model for the electrolyte which predicts a smooth DLC formation. Long protrusions are electrically “singular”, which violate the assumption of a spatially uniform electrolyte.

Currently, UC modeling is still in its early stages. There is no systematic way to identify device resistance, capacitance, and inductance values of a carbon nano-tube ultra-capacitor (CNU) from the electrolyte ionic information or the device geometrical features. Many existing UC modeling studies [35-37] simply aim to recover the measured impedance as a function of frequency, i.e., express Nyquist characteristics using an empirical equivalent circuit for traditional UCs with smooth corrugations. The impedance of the CNU with long CNT cylinders protruding on electrode surfaces cannot be systematically determined using equivalent circuit models. Changes in the UC structure or the electrolyte mass and/or volume density is equivalent to those in the resistance, inductance, and capacitance of the UC model, and empirical equivalent circuit models cannot meet this objective. Thus the existing UC models are not adequate for our study. To mitigate the scarcity of such approach, we have recently developed a particle-based physical model, using molecular dynamics [1,38-39], which yielded results that compared well with existing experimental data [40]. Such a model enables us to calculate the electric field between the electrodes, keep track of the electrolyte ionic motion in the capacitor, and evaluate the device parameters and performance under an arbitrary set of geometrical parameters, electrolyte properties, and voltage excitation.

Following the development of our molecular dynamics (MD) algorithm in [1], we apply this model to investigate the relationship between CNU capacitance and electrode geometry [41]. In particular, we examine the dependence of CNU linear capacitance density CD_L (in farad per unit electrode width) on electrode-to-electrode separation L_y , CNT length L_{CNT} , and CNT linear packing density D_{CNT} (ratio of CNT diameter d to CNU cell width W_C), and compare our simulated results with available experimental data [42]. Our results show that there is an optimal D_{CNT} range above

which CD_L drops dramatically, even below that of the equivalent parallel-plate capacitor (when $L_{CNT} = 0$). This behavior is attributed to the formation of an electrolyte ionic trap near the CNT base, which occurs at a CNT-to-CNT separation of approximately $\left(\frac{2}{3}\right) L_{CNT}$. The proximity of CNTs at this separation creates too large a potential barrier between adjacent CNTs for the electrolyte ions to overcome, which are in turn trapped and prevented from participating in the formation of a DLC. This and other findings reported here serve to enhance our understanding of the CNU performance that can lead to development of necessary guidelines for eventual CNU cell design.

In this dissertation we present in detail the modeling of a CNU cell. In Chapter 2 we describe in a detail the theoretical basis of our simulation methodology along with the proper theoretical background governing our model. We define and describe the simulation unit cell and provide the proper scaling relationships between a real CNU cell and our computational model. We define the coulomb interactions of the electrode and electrolyte particles in the computational unit cell and describe the proper boundary conditions to ensure conservation of energy in the unit cell during the transient simulation. We continue to describe the total current in the model and provide a detailed derivation of the scaling relationships of the velocity, electrolyte collision period, resistance, time and frequency that bound our model. In Chapter 3 we continue to use the aforementioned definition of our computational cell and use the methodology to extract a cyclic voltammetry (CV) and a Nyquist plot and compare that to existing experimental data. We show that the electrical behavior of a CNU can be described by electrolyte polarization and ionic spatial distributions in the capacitor volume. We also proceed to suggest electrical equivalent circuit models of the CNU. In Chapter 4 we continue to develop the proper criteria for CNU cell design. We examine geometrical dependencies like the electrode-to-electrode separation, the

CNT length and the CNT density as well as the effect of scan rate on the CNU capacitance density.

We conclude by paving the way to future work as well as a detailed explanation of the computational algorithm describing the CNU cell.

References

- [1] A. Orphanou, T. Yamada, C. Y. Yang, *Nanotechnology* **23**, 095401 (2012)
- [2] S. Pang, M. Anderson, T. Chapman, *J. Electrochem. Soc.* **147**, 444 (2000)
- [3] S. Gupta, M. Hughes, A. H. Windle, J. Robertson, *J. Appl. Phys.* **95**, 2038 (2004)
- [4] G. Zhou, D. Wang, F. Li, L. Zhang, Z. Weng, H. Cheng, *New Carbon Mater.* **26**, 180 (2011)
- [5] D. Tashima, M. Taniguchi, D. Fujikawa, T. Kijima, M. Otsubo, *Mater. Chem. Phys.* **115**, 69 (2009)
- [6] H. Wang, H. Dai, *Chem. Soc. Rev.* **7**, 2473 (2013)
- [7] E. Frackowiak, F. Beguin, *Carbon* **39**, 937 (2001)
- [8] R. Koetz, M. Carlen, *Electrochem. Acta* **45**, 2483 (2010)
- [9] A. Balducci, R. Dugas, P. L. Taberna, P. Simon, D. Plée, M. Mastragostino, S. Passerini, *J. Power Sources* **165**, 9222007
- [10] E. Frackowiak, K. Jurewich, K. Szostak, S. Delpeux, F. Beguin, *Fuel Proc. Tech.* **213**, 77 (2002)
- [11] M. Kaempgen, C. K. Chan, J. Ma, Y. Cui, G. Gruner, *Nano Lett.* **9**, 1872 (2009)
- [12] G. R. Li, Z. P. Feng, Y. N. Ou, D. Wu, R. Fu R, Y. X. Tong, *Langmuir* **26**, 2209 (2010)
- [13] K. Babe, K. Jurewicz, *Fuel Proc. Tech.* **77–78**, 181 (2002)
- [14] Liu, Z. Yu, D. Neff, A. Zhamu, B. Jang, *Nano Lett.* **10**, 4863 (2010)
- [15] T. Yamada, Y. Yamamoto, W. A. Harrison, *J. Vac. Sci. Technol. B* **14**, 1243 (1996)
- [16] T. Yamada, *J. Vac. Sci. Technol. B* **15**, 1019 (1997)
- [17] T. Yamada, C. W. Bauschlicher, H. Partridge, *Phys. Rev. B* **59**, 15430 (1999)
- [18] M. S. Dresselhaus, G. Dresselhaus, P. C. Eklund, *Science of Fullerenes and Carbon Nanotubes* (Academic, London, 1996)
- [19] T. Yamada, *Appl. Phys. Lett.* **76**, 628 (2000)
- [20] T. Yamada, *Appl. Phys. Lett.* **78**, 1739 (2001)
- [21] T. Yamada, *Appl. Phys. Lett.* **80**, 4027 (2002)
- [22] T. Yamada, T. Saito, M. Suzuki, P. Wilhite, X. Sun, N. Akhavantafi, D. Fabris, C. Y. Yang, *J. Appl. Phys.* **107**, 044304 (2010)
- [23] Q. Cheng, T. Tang, J. Ma, H. Zhang, N. Shinya, L. Qin, *Phys. Chem. Chem. Phys.* **13**, 17615 (2011)
- [24] P. Kurzweil, M. Chwistek, *J. Power Sources* **176**, 2555 (2008)
- [25] E. Frackowiak, G. Lota, J. Pernak, *Appl. Phys. Lett.* **86**, 164104 (2005)
- [26] J. D. Stenger-Smith, C. K. Webber, N. Anderson, A. P. Chafin, K. Zong, J. R. Reynolds, *Electrochem. Soc.* **149**, A973 (2002)
- [27] H. Yamada, P. R. Bandaru, *Appl. Phys. Lett.* **104**, 213901 (2014)

- [28] H. Abruna, Y. Kiya, J. C. Henderson, *Phys. Today* **65**, 43 (2008)
- [29] R. Kötz, M. Carlen, *Electrochim. Acta* **45**, 2483 (2000)
- [30] H. J. In, S. Kumar, Y. Shao-Horn, G. Barbastathis, *Appl. Phys. Lett.* **88** 083104 (2006)
- [31] P. C. Chen, G. Shen, S. Sukcharoenchoke, C. W. Zhou, *Appl. Phys. Lett.* **94**, 043113 (2009)
- [32] J. Schindall, *IEEE Spectrum* **44**, 42 (2007)
- [33] P. Wilhite, A. Vyas, J. Tan, J. Tan, T. Yamada, P. Wang, J. Park, C. Y. Yang, *Semicond. Sci. Technol.* **29**, 054006 (2014)
- [34] R. de Levie, *Adv. Electrochem. Electrochem. Eng.*, **6**, 329 (1967)
- [35] S. Buller, E. Karden, D. Kok, R. W. De Doncker, *Proc. IEEE Ind. App. Soc. Mtng.* **4**, 2500 (2001)
- [36] T. D. Dongale, P. R. Jadhav, G. J. Navathe, J. H. Kim, M. M. Karanjkar, P. S. Patil, *Mat. Sci. Semicond. Process* **36** 43 (2015)
- [37] Hao, X. Wang, Y. Yin, Z. You, *J. Elect. Mat.* **45**, 515 (2015)
- [38] T. Yamada, D. K. Ferry, *Phys. Rev. B* **48**, 8076 (1993)
- [39] T. Yamada, D. K. Ferry, *Phys. Rev. B* **47** 6416 (1993)
- [40] K. Frackowiak, V. Metenier, F. Bertagna, F. Beguin, *Appl. Phys. Lett.* **77**, 2421 (2000)
- [41] A. Orphanou, T. Yamada, C. Y. Yang, *J. Appl. Phys.*, **119**, 214311 (2016)
- [42] J. H. Kim, K. W. Nam, S. B. Ma, K. B. Kim, *Carbon* **44**, 1963 (2006)

Chapter 2

Simulation Methodology and Theoretical Background

One of the challenges in developing a molecular-dynamics simulation environment is the approximation of the physical 3-D vertically grown CNT array with an appropriate model. In our approach, the 3-D CNT “forest” is approximated by a 2-D equivalent. The justification of this dimensional transformation is the assumption that transport is channeled only in the direction normal to the electrode’s perfectly reflecting walls at either end of the simulation cell, while neglecting transport in the transverse directions. For our study we assume vertically grown CNTs, but in general our methodology can assume any arbitrary CNT orientation with respect to the electrode walls. In addition, boundary conditions selection is critical not only in ensuring electrical interaction exists between adjacent CNT unit cells but also conservation of energy in the CNU volume that results in a stable computational process. The simulation is a two-step iterative process; first, the charge distribution on each CNT electrode is calculated using a full molecular dynamics solution, and second, the calculated electrode charge distribution is allowed to interact with the electrolyte ions yielding the desired CNU electrical characteristics. Details of the simulation methodology are described also below.

The objective of the foregoing analysis and the first part of our research, is to establish an accurate model and a set of assumptions to compute the frequency-dependent impedance of the CNU and compare it with an experimental Nyquist and CV plots. To realize such a comparison, we must scale the experimental electrolyte ion volume density N_e of 6 moles/liter of K^+OH^- and CNU dimensions to our simulated unit cell. Such scaling will also be described below. In the

second part of our research we apply the methodology to shed light in an actual cell design, with a focus on the optimization of it's structure.

The analysis of ultracapacitor operation reported in the literature thus far is largely phenomenological, using an equivalent circuit model consisting of capacitors and resistors to simply fit the measured Nyquist plot [1-8]. There are no detailed science-based models explaining how electrolyte ions move under the influence of charges on the plates, leading to the measured electrical behavior. The absence of science-based modeling makes the design and quantification of experimental variations in the UC cell at best empirical that depends heavily on trial-and-error. For successful development of such a potentially far-reaching and timely technology, modeling based on sound scientific understanding must be carried out.

In addition to the complex geometry of the CNU, the electric field singularity at the tips of the nanotube makes the direct solution (analytical or numerical) of the Poisson's equation in the capacitor cell rather challenging. With molecular dynamics [9-14], we distribute electrode charges throughout the complex CNU structure. Then we solve for the ionic motion inside the CNU and calculate the total current, thus providing us with the degrees of freedom necessary to optimize the cell design based on CNT size and density, electrode separation/size, and applied voltage.

2.1. Defining Simulation cell and Scaling Considerations

We approximate the 3-D CNT "forest" by a 2-D equivalent. This dimensional transformation preserves the volume density (using the concept of super-particle), ionic momentum and acceleration, ensemble average drift velocity, ionic collision period, and capacitor current

density. Once this set of conditions is imposed, we can then obtain $R_{sim}=R_{exp}$, $C_{sim}=C_{exp}/k_0$, and $L_{sim}=L_{exp}/k_0$, where k_0 is the scaling factor defined in Figure 2.1 (A.1) and R_{sim} , R_{exp} , C_{sim} , C_{exp} , L_{sim} , and L_{exp} are the measured and simulated CNU resistances, capacitances, and inductances, respectively. The transformation of the 3-D UC cell to a 2-D unit cell is shown in Figure 2.1 (A.1). From the scaling relations given above, frequency scales as $f_{sim}=k_0 f_{exp}$. Table I summarizes the scaling relations for all parameters used in our simulations. Keep in mind that various equivalent scaling relationships might be stated. For example, we can scale resistance but keep the collision period intact, or, equivalently we can scale the collision period but let the resistance unchanged.

During the simulation, we also need to preserve the experimental electrolyte volume density, N_e . To do so, we calculate the experimental electrolyte “one-ion volume” and scale it linearly to the simulated volume, which is assumed to be “one-ion” thick. The simulation cell thickness t_s shown in Figure 2.1 is calculated by linearly scaling the electrolyte volume density to a single ion. If N_{exp} and N_{sim} are the numbers of ions in the experimental and simulated cell volumes V_{exp} and V_{sim} , respectively, we then have $N_e = N_{exp}/V_{exp} = N_{sim}/V_{sim}$, ensuring that N_e is preserved throughout. From the definition of k_0 , we obtain $N_{exp} = k_0 N_{sim}$. To preserve the total ion mass and charge between experiment and simulation, each simulated ion (super-particle) must have mass and charge k_0 times larger than those of the ion in the experimental electrolyte ion. This infers that the number of actual ions (positive or negative) in each superparticle in the simulation cell is k_0 . Thus the drift current characteristics in the simulated unit cell are consistent with the experimental electrolyte particle density since the mass to charge ratio of the electrolyte remains constant between experiment and simulation.

Table I. Equivalent scaling relationships between an actual and a simulated capacitor cells. k_0 is the scaling factor defined graphically in Figure 2.1.

Experimental quantity	Simulation quantity
t (time)	t/K_0
τ (collision period)	τ/K_0
N_e (electrolyte vol. density)	N_e
\vec{V}_{drift} (drift velocity)	\vec{V}_{drift}
\vec{F}_{tot} (force)	\vec{F}_{tot}
f (frequency)	$f \cdot K_0$
q (charge)	$q \cdot K_0$
m (mass)	$m \cdot K_0$
R (cell resistance)	R
L (cell inductance)	L/K_0
C (cell capacitance)	C/K_0

2.2. Coulomb Interactions, Boundary Conditions and Conservation of Energy in the Unit Cell

We assume a CNT in a unit cell surrounded by rigid walls on the horizontal boundaries and periodic boundary conditions on the vertical cell boundaries, as shown in Figure 2.1 (A.1). The rigid wall serves as a reflection plane and energy is conserved during the elastic reflection. The Coulomb interaction must be treated using periodic boundary conditions. The most plausible implementation utilizes the minimum image approximation, derived from the Ewald Sum method [9, 15-20]. The periodic boundary condition will be discussed later in further detail and in brief it ensures the coupling among adjacent CNTs.

To ensure proper accounting for Coulomb interaction, two tests have been performed. First, the MD algorithm is tested with two different plasma coupling coefficients $\Gamma = e(n)/(4\pi\epsilon k_B T)$, where n the particle areal density, $k_B T$ the average kinetic (thermal) energy, and ϵ the dielectric constant. According to [20], the velocity autocorrelation of electrons in a low Γ environment decays exponentially with time but is oscillatory at high Γ . We study the cases $\Gamma_0=1.5$ (low-density) and $\Gamma_1=8.2$ (high-density), as illustrated in Figure 2.2 (A.2), and confirm the reported behaviors [9]. We have also confirmed that the electrostatic potential between the capacitor electrodes is independent of path selection. In fact, for two independent paths the electric potential energy is computed to be within 0.24% of each other. Thus the total energy is conserved in the assumed computational cell and throughout the numerical computation [9]. Figure 2.3 illustrates the conservation of energy in the coulomb interaction system used in the calculation of the aforementioned plasma coupling coefficients above. It illustrates a plot of the total energy in an electrode surrounded by purely reflective boundary conditions as a function of time. While attaining a steady state equilibrium position in the electrode, the kinetic and potential energy in the system is conserved, showing the total energy as constant throughout the computation. The coulomb interaction system used here, is exactly equivalent to the electrode representation as we have used it in our computation. Once in steady state, the electrode is allowed to interact with the electrolyte, for the computation of the total current in the capacitor volume.

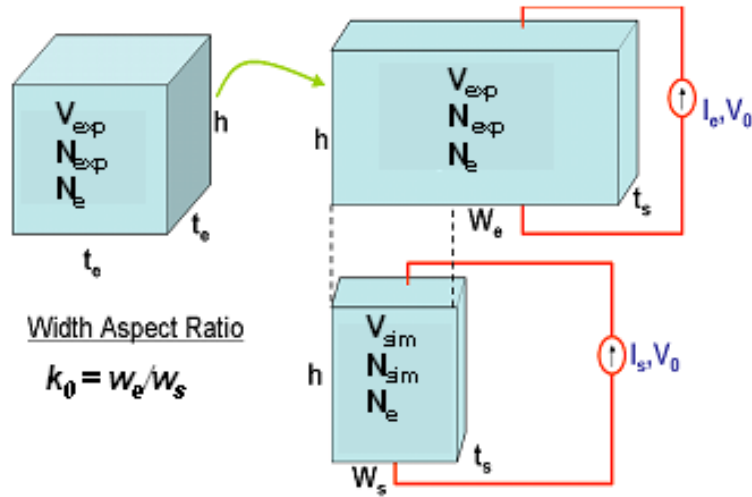


Figure 2.1. Schematic of the geometrical transformation of the actual electrolyte cell to an effective 2-D cell, which is then scaled to an equivalent 2-D simulation unit cell with scaling factor k_0 . t_s is the average electrolyte ion separation and represents the simulation cell thickness. The 3-D cell width w_e is determined from $w_e t_s = t_e^2$. The electrolyte ion volume density in the actual cell, $N_e = 6$ moles/liter, is preserved during this transformation. N_{exp} and N_{sim} are the number of ions in the actual and simulated cell volumes, respectively. The simulation cell dimensions are $w_s = 1.5 \mu\text{m}$ and $h = 3 \mu\text{m}$.

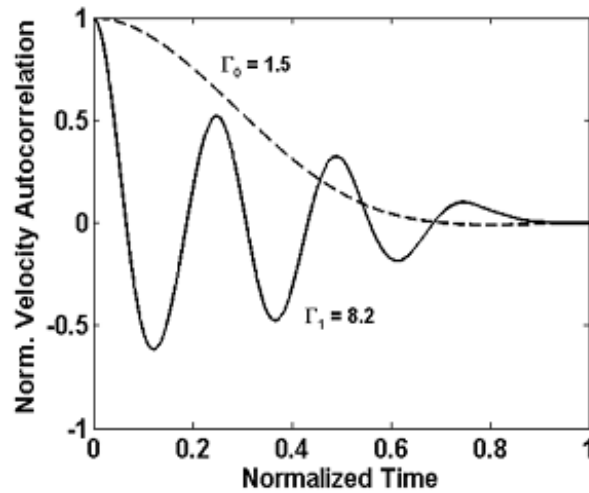


Figure 2.2. Simulated results for a system of negatively charged ions surrounded by periodic boundary walls. The normalized velocity autocorrelation of the electrons in the system is calculated as a function of time for two different ionic areal densities with ratio $n_0/n_1 = 10000$. The time scale is normalized to 0.1 ps for Γ_0 and to 10 ps for Γ_1 [24].

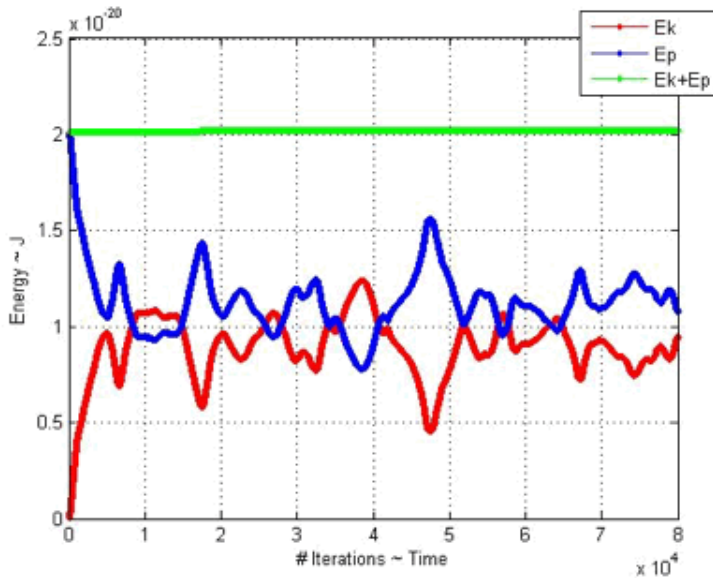


Figure 2.3. Simulated results for a system of negatively charged ions surrounded by periodic boundary walls. The system is equivalent to the plasma coupling coefficient of I_0 as described above. The kinetic energy is shown in red, the potential energy in blue and the total energy is green colors.

2.3. Particle Dynamics in the Unit Cell

The unit cell is filled with the electrolyte, KOH, and an AC voltage is applied across the electrodes. The total current density (J_{tot}) is then calculated as the time and ensemble averages of the electrolyte drift current ($J_{drf\ tot}$) plus the displacement current between the CNU electrodes ($J_{dsp.}$), with the total drift component expressed as $J_{drf\ tot} = J_{drf}(K^+) - J_{drf}(OH^-)$ in $J_{tot} = J_{drf\ tot} + J_{dsp.}$. The field created by the CNT electrodes is determined by separately analyzing the electrodes in a damping MD mode [9-14,24]. Therefore, the applied voltage is manifested as electrode charges fixed at designated locations and each charge oscillates as $q(t) = q_0 \cos(\omega t)$. Figure 2.4 shows the electric field lines and normalized potential contours in the capacitor for an electrode

charge distribution at 0.6 V. The CNT and the capacitor horizontal metallic walls are equipotential surfaces.

We employ the concept of “super-particle”, a massive and highly-charged ion. Under this assumption, the total force on the massive super-particle is determined by the applied voltage and the total friction in the electrolyte. Starting from the total force on a single ion, we formulate the equations of motion for the super-particle as follows.

$$\vec{F}_i = m_i \vec{A}_i = q_i \vec{E}_i - \frac{m_i \vec{v}_i}{\tau} + \sum_j \frac{e^2}{4\pi\epsilon R_{ij}^3} \vec{R}_{ij} \quad (2.1)$$

$$\sum_i \vec{F}_i = \sum_i m_i \vec{A}_i = \sum_i q_i \vec{E}_i - \sum_i \frac{m_i \vec{v}_i}{\tau} + \sum_{i \neq j} \sum_j \frac{e^2}{4\pi\epsilon R_{ij}^3} \vec{R}_{ij} \quad (2.2)$$

$$\vec{F}_{tot} = Q \vec{E}_{av} - \frac{M \vec{v}_{av}}{\tau}, \quad Q = k_0 q_i, \quad M = k_0 m_i \quad (2.3)$$

Here τ is the collision period in the electrolyte, \vec{v}_{av} the center of mass velocity, \vec{v}_i the drift velocity, m_i the electrolyte-ion mass, q_i the electrolyte-ion charge, \vec{A}_i the electrolyte-ion acceleration, \vec{E}_i the electric field strength, \vec{F}_i the electrolyte-ion force, Q the center-of-mass charge, M the super-particle mass, \vec{E}_{av} the center-of-mass electric field, and \vec{R}_{ij} the electrode-to-electrolyte-ion distance, with (i, j) being the superparticle index. Equation 2.1 describes the general force equation on a single particle. In Equations 2.2 and 2.3, the electrolyte electric Coulomb force does not influence the center-of-mass motion of the super-particle. The total force on the electrolyte ions given by Eq. (2.3) consists of contributions only from the electric field and dynamic friction, the latter being the electrolyte resistance. The last term in Eq. (2.2)

vanishes in the limit of a very large super-particle, $k_0 \rightarrow \infty$. From the variables defined above, τ and k_0 are the only required input to the MD simulation and are obtained from experiment [21]. τ is extracted from the real part of experimental Nyquist plots. The simulation is performed in a time-domain iterative process during which the total force per electrolyte particle is calculated based on the electrode applied voltage acceleration and electrolyte friction deceleration, with the new displacement computed accordingly. Thus the total current in the CNU cell is computed for a given voltage, from which the impedance characteristics are obtained.

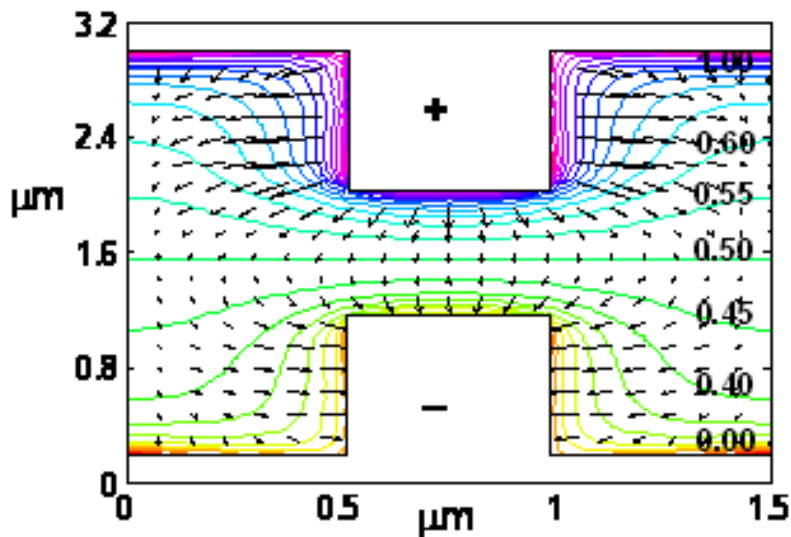


Figure 2.4. Normalized potential contour plot and electric field lines in the simulated CNU cell for OCV = 0.6 V. The top electrode is positively and the bottom electrode is negatively charged.

2.4. Boundary Conditions in the Unit Cell

One of the key features of our MD algorithm is that we can allow electrical interaction of neighboring CNTs in the computational cell. That is a key and imperative feature of our computational algorithm that not only enables a realistic model representation of a CNU but also

paves the prospect of a successful correlation to an experiment. The CNT to CNT interaction is implemented through a periodic boundary condition that truncates the computational cell on the east/west boundaries of the computational cell. What the periodic boundary actually does, it allows allows electrolyte particles that transverse through it on one side of the computational cell to appear on the other side of the computational cell as if the truncated periodic boundaries of the computational cell were connected together. This spatial transformation of the electrolyte particles through the periodic boundary conditions conserves both the kinetic and the potential energy of the particles. In brief the periodic boundary condition can be described as: $\vec{v}\{\vec{R} + \vec{w}\} = \vec{v}\{\vec{R}\}$, with a spatial transformation of the electrolyte ion given by: $(\vec{R} + \vec{w}) \Rightarrow \vec{R}$, where \vec{v} the electrolyte particle velocity, \vec{R} the electrolyte particle position and \vec{w} the size of the computational cell (or the distance between the periodic boundary conditions). These conditions conserve linear momentum and hence conserve the total energy in the CNU system. The boundary condition here is consistent with the minimum image approximation method as dictated by the Ewald sum, and conserves the momentum of the ionic particles participating in the simulation [15-20, 9].

In addition to the periodic boundary condition to the east/west of the computational cell, the proper boundary condition is imperative to be selected for the electrolyte/electrode interface. To preserve the energy of the electrolyte ions that bounce on the electrode walls, we employ a perfect reflecting wall. When an electrolyte ion hits an electrode, it bounces back perfectly by retaining both it's kinetic and potential energy at the point of impact. The reflecting boundary condition can be simply described by the following velocity and spatial position relationships: $\vec{v}\{\vec{R}\} = -\vec{v}\{\vec{R}\}$, with the electrolyte ion spatial position unchanged:

$\vec{R} \equiv \vec{R}$. Similar to the periodic boundary condition for the east/west of the computational cell, the perfect reflecting electrode walls to the north/south of the computational cell conserve the total linear momentum and hence the total energy in the CNU system.

2.5. Total Current in the Simulation Unit Cell

In this section we demonstrate the theoretical model for the total current in the capacitor volume, in order to justify our computational results. Let's start with the equation of the total drift current density \vec{J} in the capacitor volume as a function of the electrical conductivity σ of the electrolyte, the electric field \vec{E} between the capacitor electrodes, the free electrolyte charge in the capacitor volume ρ_f , and the velocity of the free electrolyte charge \vec{v} .

$$\vec{J} = \sigma \vec{E} + \rho_f \vec{v} \quad (2.4)$$

The first term in the total current above represents the conduction component of the drift current and the second term is somewhat analogous to convection due to motion of charges in the CNU volume.

Next, let us consider the equation of motion of the free electrolyte charges in the presence of the electrode applied voltage, where m is the electrolyte ion mass and τ the collision period between electrolyte ions in the presence of the electrode applied electric field \vec{E} .

$$m \frac{\partial \vec{v}}{\partial t} = q \vec{E} - \frac{m \cdot \vec{v}}{\tau} \quad (2.5)$$

The first term on the right side of Equation 2.5 is the electrostatic force and the second term the friction force. Taking now the Fourier transform of the equation of motion (Equation 2.5) above and solving for the electrolyte drift velocity phasor $\vec{v}(\omega)$ we get,

$$\vec{v}(\omega) = \frac{q\vec{E}(\omega)(1+j\omega\tau)}{\frac{m}{\tau}(1+\omega^2\tau^2)} \quad (2.6)$$

Substituting now the above (Equation 2.6) into the total current given in Equation 2.4, we get the total convection current density in the capacitor volume as a function of the angular frequency (ω),

$$\vec{j}_f(\omega) = \left(\sigma - \rho_f \frac{q}{\frac{m}{\tau}(1+\omega^2\tau^2)} \right) \cdot \vec{E}(\omega) + \rho_f \frac{j\omega q\tau}{\frac{m}{\tau}(1+\omega^2\tau^2)} \vec{E}(\omega) \quad (2.7)$$

At the low frequency limit, the equation above becomes

$$\vec{j}_f(\omega) = \left(\sigma - \rho_f \frac{q\tau}{m} \right) \cdot \vec{E}(\omega) + \rho_f \frac{j\omega q\tau^2}{m} \vec{E}(\omega) \quad (2.8)$$

Where the first term in the equation above represents ohmic resistance, and the second term a capacitive reactance. Therefore, at the low frequency limit, the computational CNT cell can be represented with a resistor in series with a capacitor ($R + \frac{1}{j\omega C}$). On the other hand, at the high frequency limit, the total current density in the capacitor is represented by

$$\vec{j}_f(\omega) = \left(\sigma - \rho_f \frac{q}{(\omega^2 \cdot \tau \cdot m)} \right) \vec{E}(\omega) + \rho_f \frac{q}{(j\omega m)} \vec{E}(\omega) \quad (2.9)$$

which is nothing but an ohmic current term in series with an inductive reactance. As a result, the high frequency limit impedance response of the CNT cell is just a resistor in series with an inductor ($R + j\omega L$).

Therefore, our algorithm is consistent with the theoretical current expected behavior and can recover the full electrical parameters of a CNU cell using just ionic movement and distributions in the capacitor volume. Ionic movement alone can recover the electrical properties of the capacitor model.

A special case of total current exists in the capacitor volume when the capacitor is fully charged. When this condition exists full screening between the electrode and electrolyte in the capacitor volume exists and therefore the convection current $\rightarrow 0$. Therefore the equation of the total current needs to be re-examined. Rewriting Equation 2.4 with the addition of a displacement current density term,

$$\vec{J} = \sigma \vec{E} + \rho_f \vec{v} + \varepsilon_0 \frac{\partial \vec{E}}{\partial t} \quad (2.10)$$

where ε_0 the permittivity of free space. When the electrolyte ions are drifting in the capacitor volume then $\sigma \cdot \vec{E} + \rho_f \cdot \vec{v} \gg \varepsilon_0 \cdot \frac{\partial \vec{E}}{\partial t}$ and Equation 2.4 persists, with the drifting component of the total current being the dominating current component. When the capacitor is fully charged then the double layer potential dominates, with the convection current $\rightarrow 0$ and therefore the total current is dominated by the double layer displacement current as shown from Equation 2.4, $\sigma \cdot \vec{E} + \rho_f \cdot \vec{v} \ll \varepsilon_0 \cdot \frac{\partial \vec{E}}{\partial t}$.

With the addition of the double layer displacement current we complete the equation for the conservation of the total current in the capacitor volume [22]. Figure 2.5 below, graphically illustrates the computation of the drift and displacement current components in the extraction of a sample cyclic voltammetry plot. The ramp applied voltage in the extraction of a CV plot is very slow to capture a full charging and recharging cycle of the CNT capacitor model and as such, the total current is dominated by the displacement current.

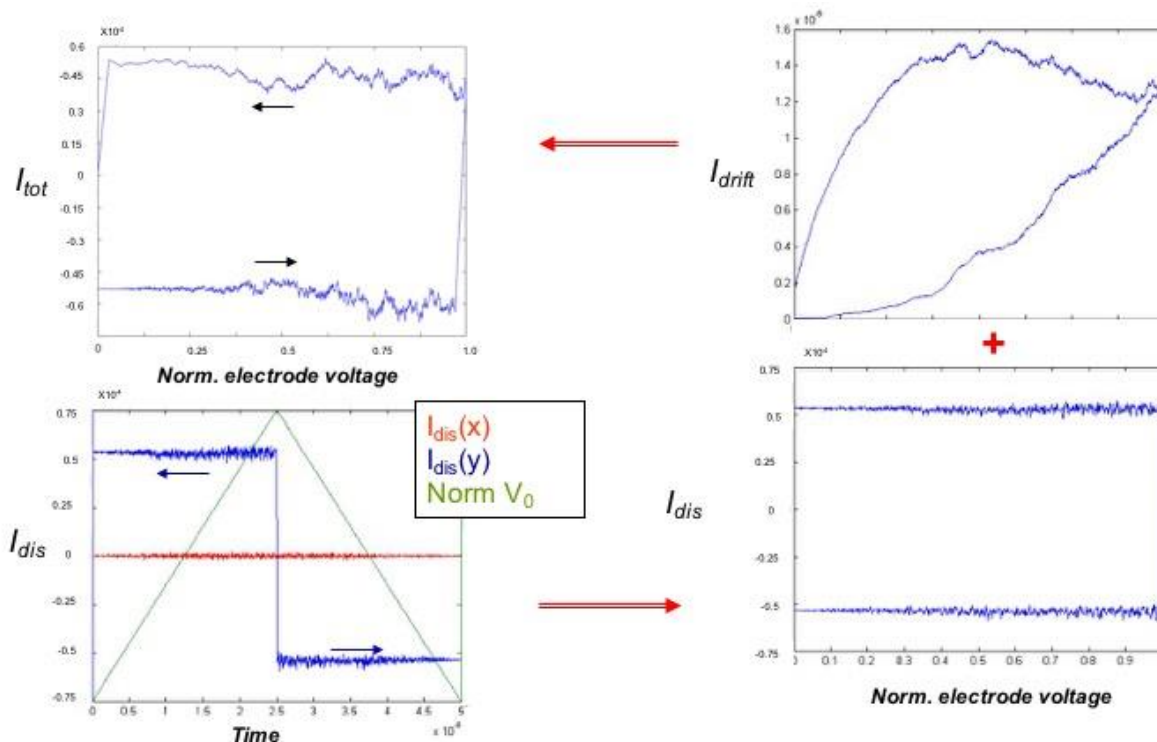


Figure 2.5. Illustration of the total current calculation and the current constituents in the computation of a Cyclic Voltammetry plot within the computational cell. The total current is the summation of the convection and the displacement currents in the capacitor volume.

2.6. Derivation of Scaling Relationships Between Simulated and Real CNU Cell

In this section we give a detailed derivation of the scaling relationships used in the modeling of a CNU. These relationships aim to scale the simulated model to an experimental CNU cell. The computational resource limitations of such a problem can not allow for an unlimited number of particles in the MD algorithm. As such we lump the electrolytes into a finite number of super-particles in order to preserve the electrolyte volume density between the simulated model and the experimental CNU cell. Below we examine how the concept of the super-particle scales the physical parameters of the CNU cell.

2.6.1. Velocity Preservation

We start by defining the total force on a super-particle $Q = K_0 q_e$ where K_0 the size of the super-particle and q_e the individual electrolyte particle charge. The total force on the electrolyte particles due to the electrode voltage source is hence given by:

$$\vec{F}_{tot} = K_0 \left(\frac{q_e q_s}{4\pi\epsilon_0 |R|^2} \hat{a}_R - \frac{q_e}{\tau} \vec{v}_d \right) = K_0 \vec{F}_r \quad (2.11)$$

Where, \vec{F}_{tot} is the simulated total force on an individual electrolyte particle, q_s the electrode charge acting upon the electrolyte particle q_e , \vec{v}_d the velocity of the electrolyte particle, τ the electrolyte collision period in the capacitor volume and \vec{F}_r the equivalent experiment equivalent force acting on the electrolyte q_e . Using the above equation, the partial velocity $\vec{\Delta v}_e$ on the electrolyte particle q_e can be expressed as:

$$\vec{\Delta v}_e = \frac{\vec{F}_{tot}}{K_0 m_e} \Delta t = \frac{\vec{F}_r}{m_e} \Delta t \quad (2.12)$$

where m_e the individual electrolyte particle mass. Here we observe that the implementation of the super-particle in the computational algorithm preserves the drift velocity of the electrolyte particles between a real CNU case and the computational unit cell.

2.6.2. Electrolyte Collision Period and Resistance Preservation

Next we consider how the electrolyte collision period τ_e and the cell resistance R_s of the simulated unit cell are preserved due to the presence of the super-particle. We first define the electrolyte collision period in the simulation unit cell as

$$\tau_e = \left(\frac{1}{R_s} \right) \left(\frac{L_e}{A_e} \right) \left(\frac{1}{n_e} \right) \left(\frac{m_e}{q_e^2} \right) \left(\frac{1}{K_0} \right) = \frac{\tau_r}{K_0}, \quad (2.13)$$

where L_e the the distance between the electrodes and A_e the area of the electrode. Both L_e and A_e are preserved between the simulation and the experiment, and n_e is the electrolyte volume density. From the above equation we choose to preserve the resistance R_s between the experiment and the simulation and that is exactly equivalent to scaling the experimental collision period τ_r in our simulation by a super-particle factor of K_0 .

2.6.3. Time and Frequency Scaling.

We rewrite the electrolyte particle, q_e , partial velocity in eq. 2.12 as

$$\overrightarrow{\Delta v}_e = \frac{\vec{F}_{tot}}{m_e} \left(\frac{\Delta t}{K_0} \right) = \frac{\vec{F}_{tot}}{m_e} \widetilde{\Delta t} \quad (2.14)$$

Where Δt the real time as observed in an experimental setup and $\widetilde{\Delta t}$ the simulated scaled time.

We have already shown and established that the velocity of the electrolyte and total force \vec{F}_{tot} is preserved between the real measurement and our computational model. In addition to that, from the above time-relationship we see that the simulated scale time is K_0 times smaller than the actual real time or equivalently, the experimental frequency is K_0 smaller than the simulated model frequency. Therefore, to recover the proper correlation data the simulated unit cell needs to run at a frequency K_0 times larger than that of the experiment.

References

- [1] L. Zhang, Z. Wang, X. Hu, F. Sun, D. G. Dorrell, *Journal of Power Sources* **274**, 899 (2015)
- [2] R. A Dougal, L. Gao, S. Liu , *Journal of Power Sources* **126**, 250 (2004)
- [3] T. Wei, X. Qi, Z. Qi, *Electrical Machines and Systems conf.* **69** (2007)
- [4] N. Bertrand, J. Sabatier, O. Briat, J.M. Vinassa, *IEEE Trans. Ind. Electron.* **57**, 3991 (2010)
- [5] J.N. Marie-Francoise, H. Gualous, A. Berthon, *IEEE Proc. Electr. Power Appl.* **153**, 255 (2006)
- [6] H. Michel, *J. Power Sources* **154**, 556 (2006)

- [7] J. Farahmandi, *Electrochem. Soc. Proc.* **25–96** 167 (1996)
- [8] E. Frackowiak, K. Metenier, V. Bertagna, F. Beguin, *Appl. Phys. Lett.* **77**, 2421 (2000)
- [9] T. Yamada, D. K. Ferry *Phys. Rev. B* **47**, 6416 (2000)
- [10] P. J. Price, “in *Fluctuation Phenomena in Solids*”, edited by R. E. Burgess (Academic, New York, 1965), pp. 355-380
- [11] B. J. Alder, T. E. Wainright, *Phys. Rev. A* **1**, 18 (1970)
- [12] J. P. Hansen, D. Levesque, J. J. Weis, *Phys. Rev. Lett.* **43**, 979 (1979)
- [13] C. Jacobini, L. Reggiani, *Rev. Mod. Phys.* **65**, 645 (1983)
- [14] J. Hardy, O. de Pazzis, Y. Pomeau, *Phys. Rev. A* **13**, 1949 (1976)
- [15] M. J. Gann, A. M. Kriman, D. K. Ferry, *Phys. Rev. B* **41**, 12659 (1990)
- [16] M. P. Allen, D. J. Tildesley, *Computer Simulation of Liquids* (Clarendon, Oxford, 1987)
- [17] D. J. Adams, G. S. Dubey, *J. Comp. Phys.* **72**, 156 (1987)
- [18] T. Darden, D. York, L. Pedersen, *J. Chem. Phys.* **98**, 10089 (1993)
- [19] U. Essmann, L. Parera, M. L. Berkowitz, T. Darden, H. Lee, L. G. Pedersen, *J. Chem. Phys.* **113**, 8577 (1995)
- [20] T. Yamada, D. K. Ferry *Phys. Rev. B* **47**, 6416 (1993)
- [21] E. Frackowiak, F. Beguin, *Carbon* **39**, 937 (2001)
- [22] K. Kontturi, L. Murtomaki, *Ionic Transport Processes: In Electrochemistry and Membrane Science*, (Oxford University Press, 2008)

Chapter 3

Simulation of CNU Cell Using Molecular Dynamics

In Chapter 2.2 we have described a set of elementary test for the coulomb interactions in our Molecular Dynamics algorithm. In this chapter we will proceed to test our Molecular Dynamics algorithm with an application on a CNT electrode capacitor cell. Our goal is to extract basic fundamental quantities of the simulation cell and compare it with experimental data. In the study of UCs, the Cyclic Voltametry (CV) plot and the Nyquist plots are elementary characteristic of a capacitor. The former, CV plot, indicates the ability of the capacitor to retain charge and it is a plot of the capacitance density in the capacitor over a ramp applied voltage at the electrodes. The more-square the CV-plot is in shape, the better the capacitance of the CNT structure. The later plot, the Nyquist plot, is a plot of the supercapacitor impedance as a function of the capacitance density and frequency and it indicates the range of frequencies over which the structure is capacitive.

Figure 3.1 shows the measured Nyquist plots for a CNU at two applied voltages. Our simulation results are also shown on the same Figure, and will be discussed in the Results and Discussion section. A Nyquist plot displays the capacitor's frequency-dependent reactance $-\text{Im}(Z)$ as a function of resistance $\text{Re}(Z)$, with the applied voltage frequency as a parameter. The plot was obtained from Electrical Impedance Spectroscopy (EIS) measurements for a CNU consisting of a 6 moles/liter KOH electrolyte solution subject to an applied voltage [1].

Figure 3.2(a) shows the experimental CV plot for the same capacitor obtained using a voltage sweep rate of 1 mV/s [1]. It displays the total current through the capacitor as a function

of voltage. Figure 3.2(b) illustrates the simulated CV plots for a CNU with the same electrolyte ion volume density N_e as the experimental one, which will be discussed in the Results and Discussion section. In CV measurements, the capacitor is linearly charged with time and subsequently allowed to discharge, providing information about the total capacitance and the capacitor's ability to store energy between the electrolyte ions and electrodes [1-16]. Both the CV and the Nyquist plots characterize the capacitor's electrical performance and are examined here in detail as a means of validating the application of the MD algorithm application in supercapacitors and in particular here in this study the CNU. Our goal is to show that electrolyte ionic movement and distributions in the UC volume are sufficient to characterize the UC. In addition, we proceed to fit the Nyquist plot into an equivalent capacitor RLC model/circuit.

3.1. Nyquist plot extraction and comparison to experiment

The experimental Nyquist plots shown in Figure 3.1 were obtained at open-circuit peak sinusoidal voltages (OCV) of 0.2 V and 0.6 V [1], respectively. It describes the capacitor's reactance versus resistance behavior in different frequency regimes, with the far right of the plot being the low-frequency and the left being the high-frequency impedance response. As observed from this plot, the simulated results compare well with their experimental counterparts. Using existing phenomenological models [17-24], such a direct comparison would not have been possible. In the simulation, the double layer capacitance (DLC), resulting from the electrode and the electrolyte ion charges, is used to describe the CNU behavior. The DLC has a maximum value at dc, when the electrolyte ions are closely attached to their respective electrodes. It is

responsible for the large amount of energy stored in the capacitor and is frequency-dependent, as shown in Figure 3.1.

Our simulation results reveal that the higher the OCV is, the higher the frequency at which the DLC vanishes. At higher OCVs, the electrolyte ions tend to maintain a close proximity to the electrodes, thus creating a larger DLC, which is less sensitive to frequency variations as shown in Figure 3.1. As a result, a higher frequency is required to counter the added inertia of the electrolyte ions due to the presence of a higher electrode force. In addition, our model underestimates the effect of the DLC, which is partly attributed to the absence of a hollow channel inside each CNT in the simulation model [25,26]. The straight and rigid large-diameter nanotubes used as electrodes in the experimental data [1] were obtained using chemical vapor deposition (CVD) of propylene at 800 °C within the pores of an alumina template (P800AL) and were arbitrary in orientation.

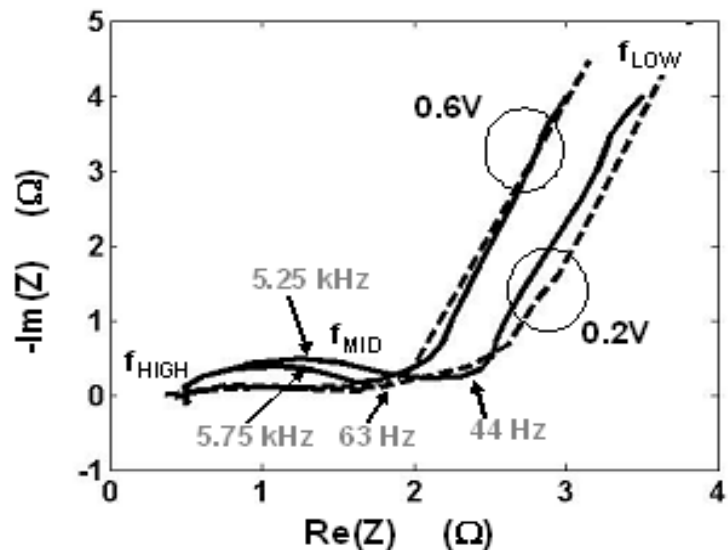


Figure 3.1. Experimental and simulated Nyquist plots for a CNU with a 6 moles/liter of KOH electrolyte at 0.6 V and at 0.2 V. Simulated and measured results are shown in dashed and solid lines, respectively. The three frequency regimes are identified by f_{LOW} , f_{MID} , and f_{HIGH} , respectively. Two points on each experimental plot are indicated by their respective frequencies [3.1].

3.2. CV plot extraction and comparison to experiment

The measured CV plot [1] at a voltage ramp rate of 1.0 mV/s is shown in Figure 3.2(a), while the simulated CV plots of the CNU cell for three different voltage ramp rates, 1.0, 1.6, and 2.0 mV/s are shown in Figure 3.2(b). The simulated results show that the displacement current in the CNU increases with increasing voltage. Overall, the simulated CV plot is qualitatively consistent with the measured data [27]. While the CV plots offer some insight into the CNU's charging and discharging characteristics, it does not provide any frequency dependence information.

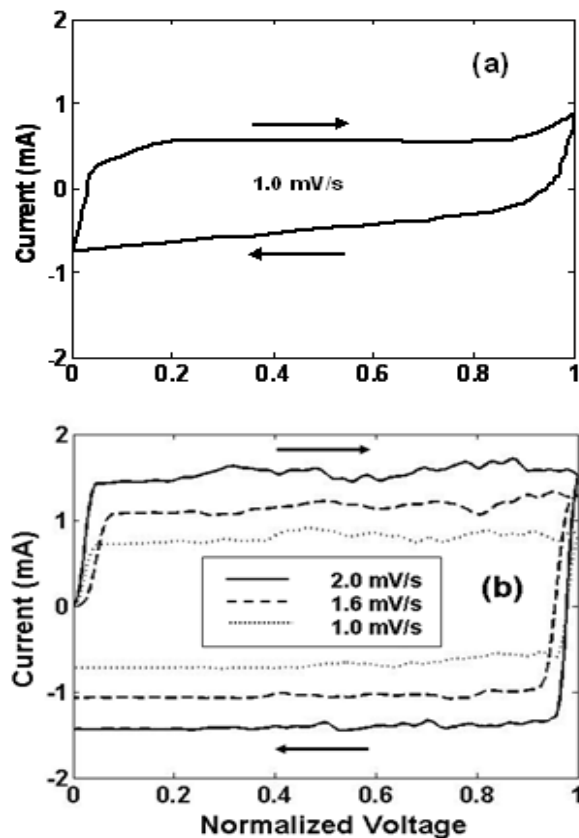


Figure 3.2. Measured and simulated CV plots. (a) Measured CV plot for electrolyte concentration of 6 mole/liter and at voltage ramp rate of 1.0 mV/s [17]. (b) Simulated CV plots for the same electrolyte concentration and at voltage ramp rates of 1.0 mV/s, 1.6 mV/s, and 2.0 mV/s, respectively.

As stated in Chapter 1, we model CNT as a solid rectangular structure which does not include the effects of the hollow interior, porosity, defects, and surface roughness. Further, we assume the electrical double layer is a result of pure Coulombic attractions between ions in the capacitor, ignoring pseudo-capacitance reactions. Nevertheless, similar to other studies [25-26], the simulated CV plot is almost rectangular in shape, suggesting that the CNT electrodes are well suited for large energy storage.

3.3. Simulation of electrolyte ionic polarization

Our primary assumption is that electrolyte ionic movement and distribution in the capacitor volume alone is sufficient for extracting the CNU electrical characteristics. The ensuing narrative describes how this is possible based on the simulated results shown in Figure 3.3.

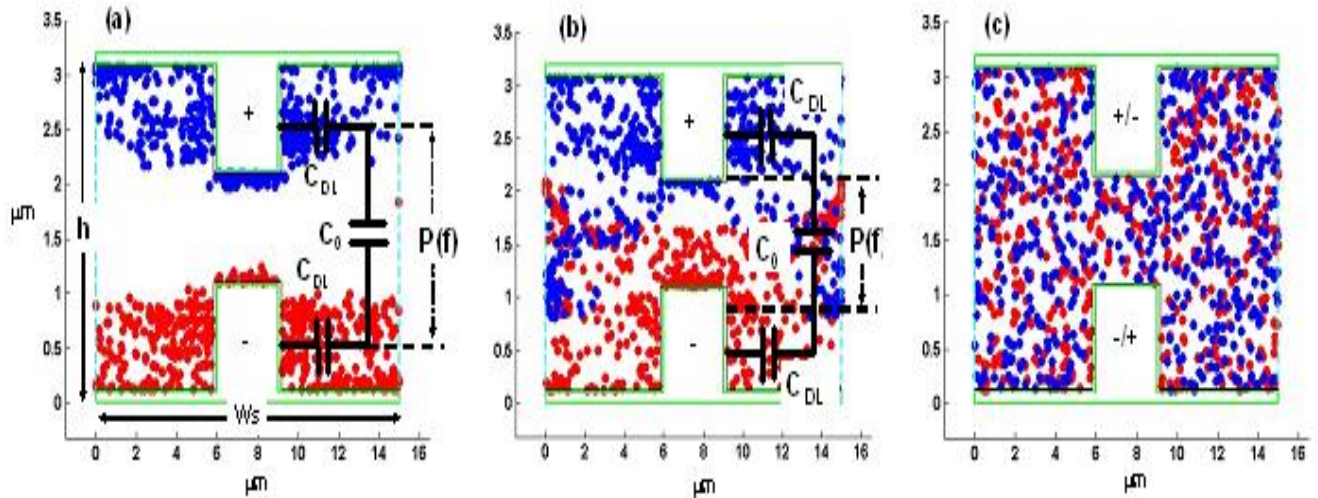


Figure 3.3. Ionic distribution snapshots at (a) low, (b) mid, and (c) high frequencies in the simulated unit cell at 0.6 V, where the CNT electrodes are situated at opposite walls of the cell indicated by green lines. Negative charges are denoted in blue and positive in red. C_{DL} is the double layer capacitance, C_0 the capacitance between the oppositely-charged electrolyte ions, and $P(f)$ the electrolyte ion average polarization distance.

At very low frequencies, electrolyte ions can screen electrode charges almost perfectly as shown in Figure 3.3(a), and maximize the double layer energy storage in the capacitor by reducing the ion-electrode separation. In this frequency region, the electrolyte ions are well separated leading to two well-defined double-layer capacitances and a maximum average free charge polarization distance, $P(f)$, as shown in Figure 3.3(a). Current continuity in the CNU is thus achieved through a strong capacitive drift convection current density, which is capacitive in nature, a “parasitic” ohmic drift current correction, and a very weak displacement current density. When $\max\{P(f)\}$ is reached at low frequencies, the electric field between the CNTs is very small, resulting in a small electrolyte-electrolyte ion capacitance C_0 and a weak displacement force. A limiting case of the low-frequency scenario is the CV plot of Figure 3.2. At an extremely slow-varying voltage approaching dc the ions are completely attached to their respective electrodes and unable to drift. In this scenario the current continuity in the capacitor volume is achieved through a displacement current and a very weak drift current correction.

At intermediate frequencies, the CNU still continues to exhibit capacitive characteristics. However, at this stage, the electrolyte ions move farther away from the electrodes, as shown in Figure 3.3(b), yielding a smaller C_{DL} . Here the electrolyte ions are at their peak drift position, farther away from the electrodes and decreasing as the capacitance decreases (the average free charge polarization distance in the capacitor volume is now smaller than in the low-frequency case). Although the capacitance due to the electrolyte ions, C_0 , is now larger, the decrease in C_{DL} is much more dramatic, resulting in an overall decrease in the total capacitance. This causes the “bump” in the Nyquist plots in Figure 3.1. C_0 is smallest at dc during which the electrolyte and electrode ions are closest to each other, maximizing the distance between positive and negative

ions and minimizing the total electric field. At intermediate frequencies, the electrolyte ions still maintain in a non-uniform distribution as shown in Figure 3.3(b), and unlike the low-frequency case, current continuity in the CNU is achieved only through a “weaker” capacitive convection current density and stronger drift current correction. At both high and intermediate frequencies, the CNU behaves like a frequency-dependent parallel RC -circuit.

At much higher frequencies the CNU displays an inductive component. The heavy electrolyte ions can no longer follow the bias changes and the electrolyte loses its dielectric ability. The total current density in the capacitor is then dominated by inductive-convection and ohmic-drift components. Due to the uniform distribution of the electrolyte ions shown in Figure 3.3c, the ability of the structure to store energy is diminished, resulting in a negligible C_{DL} . At this stage the electrolyte exhibits inductive and resistive behavior and behaves much like a series RL -circuit, because the system tends to have a voltage in the opposite direction of the current (ions are so heavy that they cannot follow the quick change in the voltage polarity at high frequency). The high-frequency CNU characteristics are of particular interest in high-speed switching applications, where high current is needed in the MHz regime. This finding further necessitates the development of a science-based model to elucidate the frequency dependence of CNU behavior.

By extracting the CNU impedance frequency response from the Nyquist plot, the impedance of the CNU is obtained as a function of frequency, as shown in Figure 3.4 (solid lines). At low frequencies, as expected, the CNU has negative (capacitive) reactance and a finite, exponentially decaying resistance value. As frequency increases, the reactance becomes positive and the CNU starts to exhibit slight inductive behavior and a frequency-independent resistance.

This resistance value corresponds to the one at the high-frequency end of the Nyquist plot in Figure 3.1.

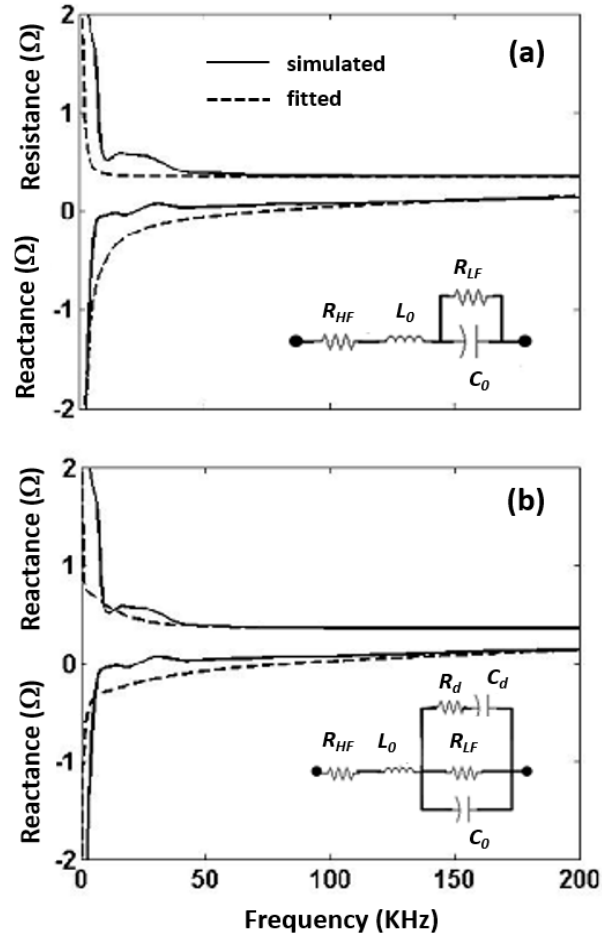


Figure 3.4. Comparison of simulated CNU impedance with that calculated using circuit models (a) and (b). The second model yields an improved fit (dashed lines) to the simulated results (solid lines). The fitted values of circuit elements are: (a) $L_0=145$ mH, $C_0=35$ mF, $R_{HF}=0.45$ Ω and $R_{LF}=18$ Ω. (b) $L_0=135$ mH, $C_0=25$ mF, $R_{HF}=0.35$ Ω, $R_{LF}=9$ Ω, $R_d=0.6$ Ω and $C_d=98$ mF.

3.4. CNU equivalent circuit

From the simulation results and following the ionic distribution discussion above, we proceed to propose two equivalent lumped-circuit models for the CNU, as given in Figure 3.4. The

impedance obtained using the first model (dashed lines in Figure 3.4a captures the resistance, inductance, and convection capacitance of the CNU. The second model (Figure 3.4b) offers a slightly better fit for both the resistive and reactive components of the impedance by incorporating additional circuit elements to account for the electrolyte dielectric absorption, R_d and C_d . In the low and mid-frequency regimes, both circuit models capture the frequency-dependent capacitive and resistive behaviors of the CNU. At high frequency, the CNU impedance is dominated by its inductance and its frequency-independent resistance.

Using a scaling scheme to model the 3-D CNU cell, we are able to simulate the capacitor operation. Our results demonstrate the importance of a science-based approach in modeling the CNU performance. We have developed a molecular dynamic algorithm that is used to compute the current in the CNU from electrolyte and CNT electrode charge distributions. The total current continuity in the capacitor is achieved through a dominant convection current component, which is capacitive in nature. At low and intermediate frequencies, the electrolyte ions have a distinct polarization which gives rise to a convection current. At high frequency the electrolyte ions polarization vanishes and the reactance becomes inductive. Further we have shown that the current continuity in the CV plot is dominated by displacement currents. This can be viewed as the limiting case of the low-frequency behavior where ions are idle and attached to their respective electrodes. We have also computed the impedance of the CNU and proposed equivalent circuit models that accurately predict the CNU performance across a wide frequency spectrum. And our simulation results compare well with existing measured Nyquist and CV plots.

Thus, the proposed MD algorithm that we have developed, successfully recovers the fundamental characteristics of a capacitor successfully.

References

- [1] Frackowiak E, Metenier K, Bertagna V and Beguin F 2000 *Appl. Phys. Lett.* **77** 2421 [3.1]
- [2] A. Orphanou, T. Yamada, C. Y. Yang, *Nanotechnology* **23**, 095401 (2012)
- [3] S. Pang, M. Anderson, T. Chapman, *J. Electrochem. Soc.* **147**, 444 (2000)
- [4] S. Gupta, M. Hughes, A. H. Windle, J. Robertson, *J. Appl. Phys.* **95**, 2038 (2004)
- [5] G. Zhou, D. Wang, F. Li, L. Zhang, Z. Weng, H. Cheng, *New Carbon Mater.* **26**, 180 (2011)
- [6] D. Tashima, M. Taniguchi, D. Fulikawa, T. Kijima, M. Otsubo, *Mater. Chem. Phys.* **115**, 69 (2009)
- [7] H. Wang, H. Dai, *Chem. Soc. Rev.* **7**, 2473 (2013)
- [8] E. Frackowiak, F. Beguin, *Carbon* **39**, 937 (2001)
- [9] R. Koetz, M. Carlen, *Electrochem. Acta* **45**, 2483 (2010)
- [10] R. Dugas, P. L. Taberna, P. Simon, D. Plée, M. Mastragostino, S. Passerini, *J. Power Sources* **165**, 9222007
- [11] E. Frackowiak, K. Jurewich, K. Szostak, S. Delpeux, F. Beguin, *Fuel Proc. Tech.* **77-78**, 213 (2002)
- [12] M. Kaempgen, C. K. Chan, J. Ma, Y. Cui, G. Gruner, *Nano Lett.* **9**, 1872 (2009)
- [13] G. R. Li, Z. P. Feng, Y. N. Ou, D. Wu, R. Fu R, Y. X. Tong, *Langmuir* **26**, 2209 (2010)
- [14] K. Babe, K. Jurewicz, *Fuel Proc. Tech.* **77-78**, 181 (2002)
- [15] Z. Yu, D. Neff, A. Zhamu, B. Jang, *Nano Lett.* **10**, 4863 (2010)
- [16] B. E. Conway, W. G. Pell *J. Solid State Electrochem.* **7**, 637 (2003)
- [17] L. Zhang, Z. Wang, X. Hu, F. Sun, D. G. Dorrell, *Journal of Power Sources* **274**, 899 (2015)
- [18] R. A. Dougal, L. Gao, and S. Liu, *Journal of Power Sources* **126**, 250 (2004)
- [19] T. Wei, X. Qi, Z. Qi, *Electrical Machines and Systems conf.* **69** (2007)
- [20] N. Bertrand, J. Sabatier, O. Briat, J.M. Vinassa, *IEEE Trans. Ind. Electron.* **57**, 3991 (2010)
- [21] J.N. Marie-Francoise, H. Gualous, A. Berthon, *IEEE Proc. Electr. Power Appl.* **153**, 255 (2006)
- [22] H. Michel, *J. Power Sources* **154**, 556 (2006)
- [23] J. Farahmandi, *Electrochem. Soc. Proc.* **167**, 25 (1996)
- [24] T. Yamada, D. K. Ferry *Phys. Rev. B* **47**, 6416 (1993)
- [25] C. Kim C and K. S. Yang *Appl. Phys. Lett.* **83**, 1216 (2003)
- [26] S. W. Lee, N. Yabuuchi, B. M. Gallant, S. Chen, B. S. Kim, P. T. Hammond and Y. Shao-Horn *Nature Nanotechnology* **5**, 531 (2010)
- [27] R. Zhou, C. Meng, F. Zhu, Q. Li, C. Liu, F. Sand, K. Jiang *Nanotech.* **21**, 345701 (2010)

CHAPTER 4

Design Criteria for CNU cell

Once we have shown that the proposed MD algorithm can successfully recover the electrical properties of a CNU [1-32], we proceed on to develop the necessary methodology to optimize vertically grown CNU geometrical features such as CNT length, electrode-to-electrode separation, and CNT packing density. The electric field and electrolyte ionic motion within the CNU are critical in determining the device performance. Using a particle-based model (PBM) based on molecular dynamics (MD) techniques we developed and reported in chapters 2 and 3, we compute the electric field in the device, keep track of the electrolyte ionic motion in the device volume, and evaluate the CNU electrical performance as a function of the aforementioned geometrical features. We show that the PBM predicts an optimal CNT density. Electrolyte ionic trapping occurs in the high CNT density regime, which limits the electrolyte ions from forming a double layer capacitance (DLC). In this regime, the CNU capacitance does not increase with the CNT packing density as expected, but dramatically decreases. Our results as you will see, compare well with existing experimental data and the PBM methodology can be applied to an ultracapacitor built from any metallic electrode materials, as well as the vertical CNTs studied in our research here.

4.1. Cell design considerations

Using the methodology reported above [1], we solve for the electric field between the nanostructured metallic electrodes. The method is essentially a Poisson equation solver using

MD based techniques with a boundary condition defined at the electrode surface, whose potential takes designated values consistent with the CNU device voltage input. We use MD to subject the device electrode charges (as a coupled system of two electrodes) to the Coulomb forces dictated by the device applied voltage and then allow them to relax to their equilibrium locations [33-39]. This is how electric field in the UCs volume is obtained. In the present PBM, we then keep track of electrolyte ionic motion as dictated by the aforementioned device electric field, and convert it to device output current. By defining the input voltage and computing the output current, it is straightforward to evaluate the device performance. It is obvious in this methodology that the electrode material can be anything as long as it is conducting. We will study CNTs for demonstration purposes, but the nanostructured electrode can be anything made of a conducting material. There are recent reports of UCs using new nanostructured electrode materials [40,41] and the methodology described here can apply to those and other UCs with different electrode materials, as we will discuss shortly below.

Our previous calculations, (chapter 3), confirmed that the electrolyte ionic motion was described successfully and yielded CNU impedance that compared well with experiment [1,3]. Using a similar approach here, we have developed a methodology that can quantify the CNU performance as a function of each of the geometrical variables, L_y , L_{CNT} , and D_{CNT} , as well as cyclic voltammetry (CV) scan rate R_{CV} [1,34]. In determining the CD_L dependence on each of the geometrical parameters, R_{CV} is kept constant.

The performance parameter in this study is the CNU CD_L . Since our model is two-dimensional, CD_L is expressed as capacitance per unit cell width, as opposed to the three-dimensional case where the capacitance density would be defined as the capacitance per unit

area. Due to the symmetry of the CNU cell and the cylindrical geometry of CNT, the choice of the transverse or horizontal component of the electric field normal to the CNT sidewall is arbitrary; hence the 2-D model is an accurate description of the CNU volume.

To examine closely the CNU behavior at high D_{CNT} , we determine the electrolyte ion spatial polarization in the CNU cell in the presence of a sinusoidal applied voltage and the electrolyte ionic distribution and electric field under CV test conditions. These tests are performed with the sole purpose of using the electrolyte ionic motion and distribution to elucidate the contribution of the electrolyte ions in the DLC formation on the electrode surfaces. Further, we compare the simulated results with experiment for two different CNUs, one having a D_{CNT} twice that of the other [3]. The electrolyte used in all simulations is equivalent to that of a 6 mole/litre K^+OH^- solution.

Defining the set of CNU design rules based on optimization of its performance is critically needed for eventual cell implementation. The results presented below elucidates how the CNU geometrical parameters affect the CNU performance and can lead to optimization of the CNU cell using a set of well-defined design rules. In particular, we report the results of CNU capacitance versus cell parameters, L_y , L_{CNT} , and D_{CNT} , and demonstrate how the simulated electrolyte ionic motion supports and elucidates the predicted CNU performance, using the methodology outlined above and particle model reported in [1].

4.2. Electrode-Electrode separation

The behavior of CD_L versus L_y is shown in Figure 4.1(a) for a unit cell with $W_C = 0.9 \mu\text{m}$, $d = 0.3 \mu\text{m}$, and $L_{CNT} = 1 \mu\text{m}$. CD_L values normalized to its maximum in the simulated unit cell [1] are

used throughout. For this unit cell, this maximum occurs at $L_y=2.2 \mu\text{m}$ (minimum L_y) with a value of 7.41 F/m. As expected, this behavior is similar to that of a parallel-plate capacitor, which is inversely proportional to L_y in the case $L_{CNT}=0$. This was a simple confirmation test and no further discussion is needed here.

4.3. CNT length

Figure 4.1(b) shows the normalized CD_L versus L_{CNT} for two cell geometries A and B, with $W_C = 0.9 \mu\text{m}$, $d = 0.3 \mu\text{m}$, and $L_y = 3.2 \mu\text{m}$ (A) and $6.2 \mu\text{m}$ (B). The maximum CD_L value of 5.12 F/m at $L_y = 3.2 \mu\text{m}$ and $L_{CNT} = 1.455 \mu\text{m}$ is used for the normalized CD_L for both A and B. We note that CD_L increases monotonically with L_{CNT} in either case, as longer CNT corresponds to larger S , which is consistent with experimental findings [42]. However, as L_{CNT} increases further and the CNT tips are closer to each other, the increase in CD_L slows, implying that the proximity of the electrodes does not yield any additional improvement in CNU performance. This behavior is attributed to the strong electric field between the CNT tips, which creates a large potential barrier for the electrolyte ions to overcome in traversing the region between the CNT tips. Thus, to avoid this region, the ions move along a path between the electrodes away from the CNT tips, where the potential barrier is lower, resulting in an effective decrease in S that offsets the increase due to a longer CNT. When this occurs, CD_L begins to saturate with further increase in L_{CNT} . As in Figure 4.1(a), where CD_L varies approximately with $1/L_y$ for a fixed L_{CNT} , the ratio of saturated CD_L values for A and B matches the reciprocal ratio of their respective L_y values, thus confirming the consistency in our simulated results.

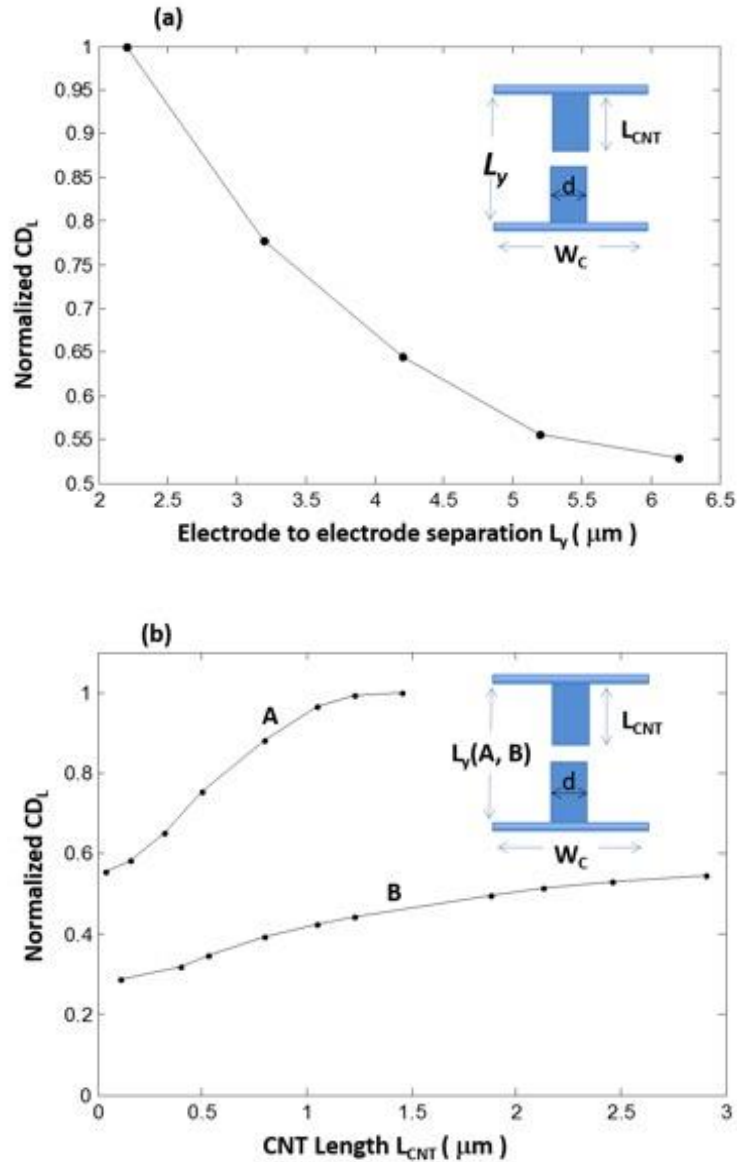


Figure 4.1. (a) Normalized simulated CD_L as a function of L_y for a CNU unit cell with $W_C=0.9 \mu\text{m}$, $d=0.3 \mu\text{m}$ and $L_{CNT}=1 \mu\text{m}$. (b) Normalized simulated CD_L as a function of L_{CNT} for a CNU unit cell with $W_C=0.9 \mu\text{m}$, $d=0.3 \mu\text{m}$ and $L_y =3.2 \mu\text{m}$ (A) and $6.2 \mu\text{m}$ (B), respectively. CNU unit cell schematic is given in inset. The simulated CD_L plot is normalized to the maximum simulated value.

4.4. CV scan rate, simulation versus experiment

To demonstrate the utility of our method, we proceed with a comparison of our simulated results with existing experimental data [43]. In particular, simulated and measured CNU

capacitances as a function of R_{CV} are compared for two capacitors, X and Y (simulated), and X' and Y' (measured), as shown in Figures. 4.2(a) and 4.2(b), respectively, where D_{CNT} for X is 0.1, twice that of Y, while X' has twice the specific surface area as Y' [43]. The vertical axis in Figure 4.2(a) is normalized to the maximum simulated CD_L evaluated at $W_C = 3 \mu\text{m}$ and $R_{CV} = 40 \text{ mV/s}$, or 35.08 F/m. The CV ramp rate peak voltage (V_0) is 1.2 V. The normalized measured capacitance density CD (in F/g) for X' and Y' versus scan rate are shown in Figure 4.2(b) [43]. Capacitor X' contains CNTs with diameters $\sim 5 \text{ nm}$ and length 10~20 nm, resulting in a specific surface area of 400 m^2/g . Capacitor Y' has CNTs 10~20 nm in diameter and 10~50 nm long, for a specific surface area of 200 m^2/g [43]. We assume that the measured capacitance density and the measured specific surface area are proportional to the linear capacitance density and linear packing density, respectively, used in our simulations. The vertical axis in Figure 4.2(b) is normalized to the maximum CD value of 110 F/g at a scan rate of $\sim 10 \text{ mV/s}$ [43]. Both simulated and experimental cells show that the capacitance density nearly doubles as the CNT density doubles, at least for low scan rates. This behavior is expected since the total capacitor area is proportional to the CNT density. However, as the scan rate increases, overcoming the inertia of the electrolyte ions results in slower DLC formation at the electrode surface, leading to decrease in capacitance density, as evidenced in both simulated and measured results, which is also consistent with experimental findings [43-46].

Based on our computed CD_L of 35.08 F/m and using the scaling rule reported previously [1], we obtain an estimated CNU energy density of 9 Wh/kg, for a 3-D unit cell volume of $W_c \times W_c \times L_y$ and multi-walled CNT on 100 nm Cu film electrodes in an electrolyte solution of 6 mole/litre K^+OH^- . This estimated energy density is within the expected range of an UC [47,48] and

comparable to the measured result for a similar CNU [18]. The energy density can be enhanced by optimizing the CNU cell geometry.

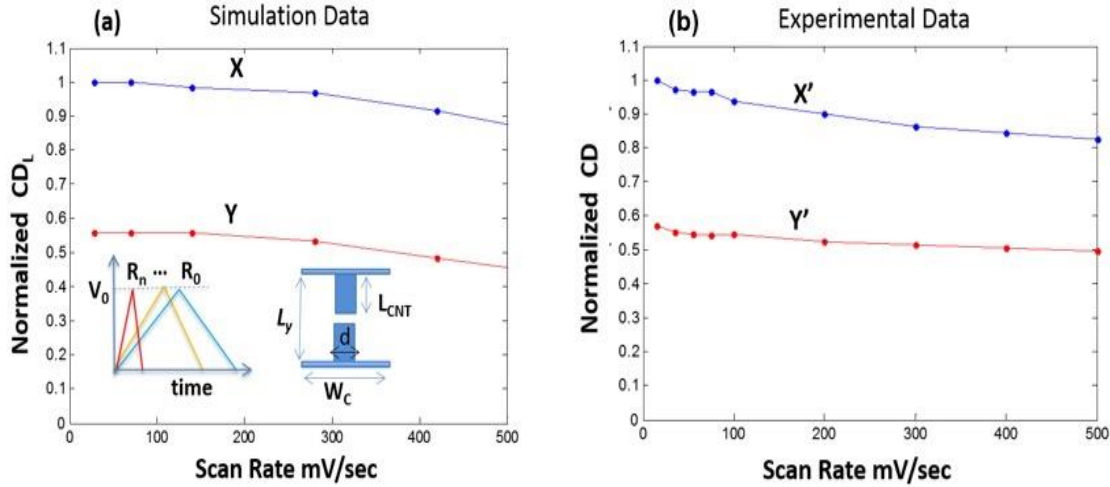


Figure 4.2. (a) Normalized simulated CD_L as a function of voltage scan rate for two CNU cells with $DCNT=0.1$ (X) and $DCNT=0.05$ (Y), respectively. The cell dimensions are: $L_y=3.2 \mu\text{m}$, $d=0.3 \mu\text{m}$, $L_{CNT}=1 \mu\text{m}$, $W_C=3 \mu\text{m}$ (X) and $6 \mu\text{m}$ (Y). (b) Normalized CD for two experimental CNU cells, with X' having twice the CNT density as Y' [43]. The simulated CD_L plot is normalized to the maximum simulated value.

4.5. Effect of CNT density on CNU performance and ionic traps

To optimize CNU performance and develop cell design guidelines, one must study the dependence of CD_L on $DCNT$. In our simulations, we consider three configurations: (1) $L_{CNT}=1 \mu\text{m}$, $d=0.3 \mu\text{m}$, $L_y=3.2 \mu\text{m}$; (2) $L_{CNT}=1 \mu\text{m}$, $d=0.6 \mu\text{m}$, $L_y=3.2 \mu\text{m}$; and (3) $L_{CNT}=1.2 \mu\text{m}$, $d=0.6 \mu\text{m}$, $L_y=3.2 \mu\text{m}$. The results are shown in Fig. 3. The CD_L values are normalized to that for the parallel-plate capacitor ($L_{CNT}=0$), or 2.56 F/m , which is also shown as a reference. The simulations are performed at $R_{CV}=35 \text{ mV/s}$ and $V_0=1.2 \text{ V}$. Figure 4.3 shows that CD_L increases monotonically with increasing $DCNT$. However, as CD_L continues to increase, we observe a dramatic drop in CD_L .

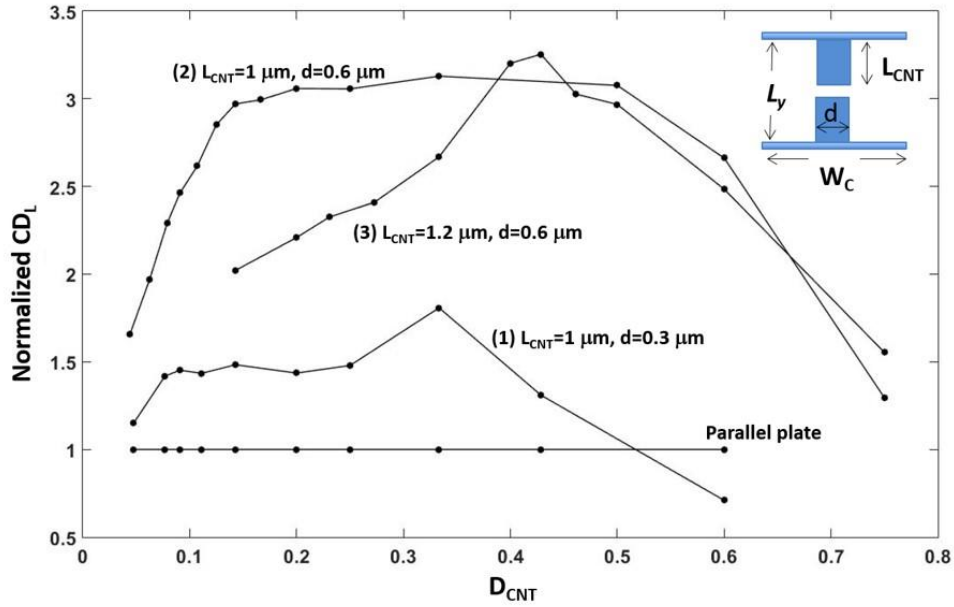


Figure 4.3. Normalized simulated CD_L as a function of D_{CNT} for three CNU configurations: (1) $L_{CNT}= 1 \mu m, d=0.3 \mu m, L_y=3.2 \mu m$; (2) $L_{CNT}= 1 \mu m, d=0.6 \mu m, L_y=3.2 \mu m$; and (3) $L_{CNT}= 1.2 \mu m, d=0.6 \mu m, L_y=3.2 \mu m$. CD_L is normalized to the equivalent parallel-plate capacitance density.

In all three configurations the sudden decrease in CD_L starts to occur when the CNT-to-CNT separation, $W_s = W_C - d$, is approximately $2/3$ the CNT length L_{CNT} . Thus, placing the CNTs at a separation less than $(2/3)L_{CNT}$, either by increasing d or decreasing W_C as D_{CNT} increases, dramatically reduces the CNU CD_L . This behavior is attributed to electrolyte ionic traps that prevent the ions from participating in the DLC formation near the electrode surface, as a result of the close proximity of the CNTs. Thus, CD_L is significantly reduced at close CNT separations. This decrease in capacitance at high CNT packing density is consistent with reported experimental data for a CNU made of single-walled CNTs [49,50].

To further examine the ionic trap formation and the decrease in CD_L at high D_{CNT} , we compare the ionic polarizations in the capacitor for two different D_{CNT} values in configuration (1), one having $W_s = 0.2 \mu m = 0.2L_{CNT}$, or high $D_{CNT} = 0.6$, and the other $W_s = 1.2 \mu m = 1.2L_{CNT}$, or low D_{CNT}

= 0.2. The two cases are labelled h and l, respectively in Figure 4.4, which illustrates the polarizations for the positive and negative ions in the electrolyte solution, as indicated by the ensemble averages of positive and negative electrolyte ion spatial distributions in the CNU cell. In this simulation, the CNU is subjected to a sinusoidal voltage with amplitude 1.2 V and period 10 s across the electrodes. As shown in Figure 4.4, the ionic polarization for high D_{CNT} is much less than that for low D_{CNT} . In the former case, the ionic distributions are confined to the mid-section between the electrodes, which in turn cannot hold a substantial amount of electrolyte charge. Thus, the DLC is diminished significantly. On the other hand, in the low D_{CNT} case, the ensemble averages for both positive and negative ions indicate that they can indeed traverse across the full distance between the electrodes, thus forming a DLC.

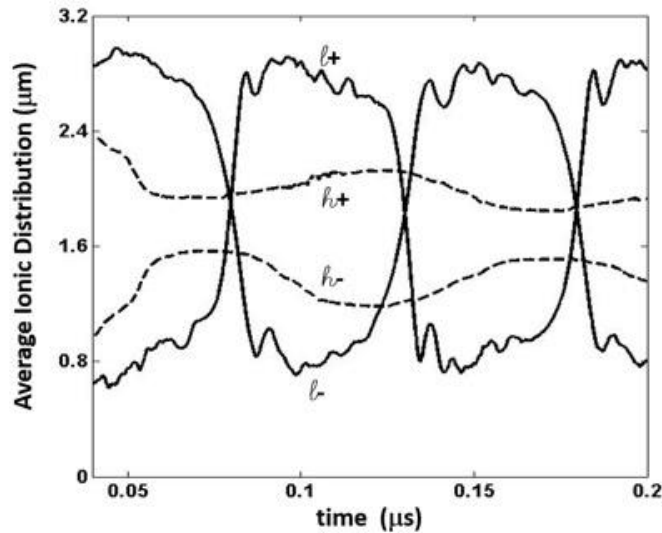


Figure 4.4. Ensemble average of electrolyte ionic spatial distributions for the positive (+) and negative (-) ions in the CNU cell, as a function of time for two different D_{CNT} values of configuration (1) defined in Figure 4. 3. They correspond to: high $D_{CNT}=0.6$ with $W_S=0.2$ $\mu\text{m}=0.2L_{CNT}$, indicated by ($h+$, $h-$) and low $D_{CNT}=0.2$ with $W_S=1.2$ $\mu\text{m}=1.2L_{CNT}$, indicated by ($l+$, $l-$).

In addition to the electrolyte polarization distances shown in Figure 4.4, we also show the ionic trap in terms of the potential well along the periodic boundaries of the computational cell to the east/west sides of the computational box that forms at high CNT densities. Figure 4.5 shows the normalized potential along the periodic boundaries between the anode and the cathode, for the two density configurations as described in the case of Figure 4.4. Figure 4.5(a) illustrates the potential “well” between the electrodes of the very high density CNT capacitor case and Figure (b) illustrates the potential of a lower density CNT capacitor. As we can see from Figure 4.5, at low CNT densities the potential is monotonic between the anode and cathode indicating that the electrolyte ions will freely transverse the capacitor volume between the two electrodes. On the contrary, in the high CNT density case illustrated in Figure 4.5(b), there exists a potential “well” between the two electrodes and it indicates that the electrolyte ions will be trapped at the point of min. potential energy.

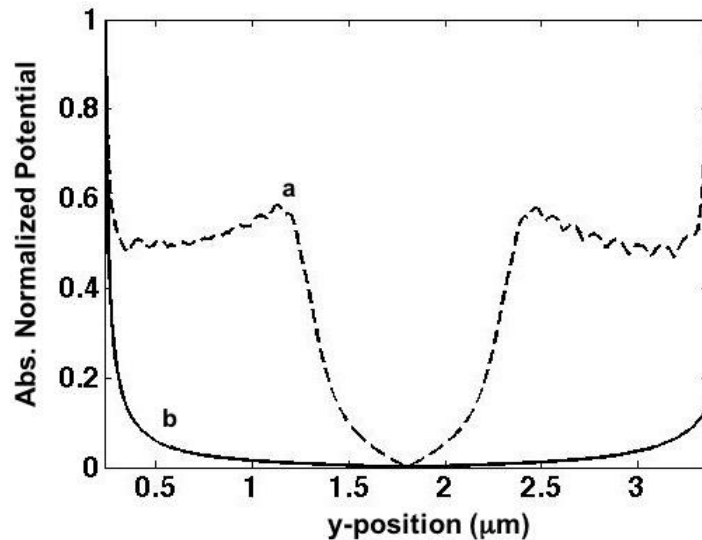


Figure 4.5. Potential energy between the anode and cathode electrodes along the periodic boundary of the computational cell for two different $DCNT$ values of configuration (1) defined in Figure 4.3. They correspond to: (a) high $DCNT=0.6$ with $W_S=0.2 \mu\text{m}=0.2LCNT$, and (b) low $DCNT=0.2$ with $W_S=1.2 \mu\text{m}=1.2LCNT$

The presence of electrolyte ionic traps at high D_{CNT} can be demonstrated with potential contour plots as well as snapshots of electrolyte ionic distribution as illustrated in Figures 4.6 and 4.7, respectively. Figure 4.6(a) shows the equipotential contours and the electric field in the capacitor for the low D_{CNT} case. The electric field E is indicated by broken lines orthogonal to the equipotential contours. Figure 4.6(b) shows a snapshot of the simulated electrolyte ionic distributions, where the positive ions are indicated in blue and negative ions in red. The potential contours in Figure 4.6(a) are consistent with the electrode surface being equipotential. The ionic distributions in Figure 4.6(b) display the formation of a DLC near the electrode surface, consistent with the polarization results in Figure 4.4.

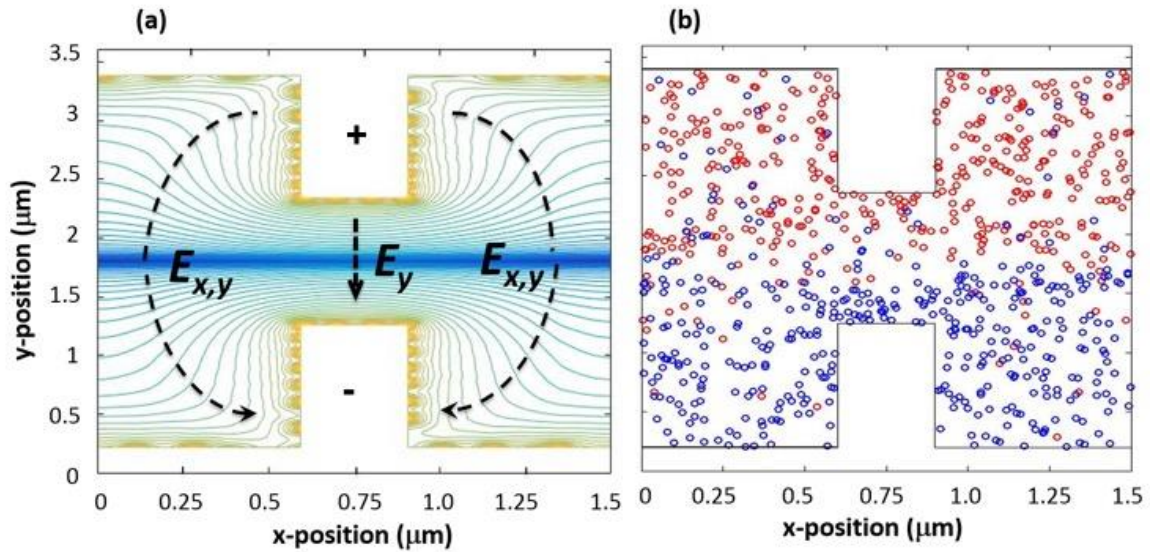


Figure 4.6. (a) Computed contours of the electric potential magnitude and the corresponding electric field in the CNU cell for configuration (1), with $W_5=1.2 \mu\text{m}=1.2L_{CNT}$ and $D_{CNT}=0.2$. (b) Time-evolution snapshot of electrolyte ionic distributions inside the same cell, where positive ions are indicated in blue and negative ions in red.

The equipotential contours and electric field for the high D_{CNT} case are displayed in Figure 4.7(a), while Figure 4.7(b) shows a similar snapshot of the electrolyte ionic distribution as in the low D_{CNT} case. The results demonstrate that the proximity of adjacent CNTs has significantly impacted the electrical behavior of the CNU. The electric field shown in Figure 4.7(a) has a large horizontal or E_x component, consistent with ionic trap formation between adjacent CNTs, where the magnitude of potential is low. This phenomenon is also consistent with the assertion that the low potential between adjacent CNTs serves to trap the electrolyte ions and restricts their movement, as evident in the snapshot of ionic distributions in Figure 4.7(b).

Due to computational limitations, solution of Poisson equation is approximated by a finite number of electrode charges. The more charges used in the electrode molecular dynamics computation, the closer to a continuous electrode charge distribution is achieved. As a result, very close to the electrodes, the computed electric field might not display the expected behavior of being normal to the electrode surface, as shown in Figures 4.6(a) and 4.7(a). However, it is demonstrated in similar computations [32,33,51] that such approximation does not affect the principal findings, since in part, in our computational model the electric field is properly restored quickly close to the electrode surface.

Our results can generally apply to any UCs with nanostructured electrodes. This is due to the structure of the computational algorithm and the way it solves for the electric field within the CNU. Different electrode materials simply reduce to a problem solution of the Poisson equation employing the same boundary conditions along the electrode boundary. As long as the electrode is metallic enough, the electric field within the UC volume is independent of the electrode material. Although CNUs are considered and analyzed as an example for demonstration

purposes, our simulation method and results can generally apply to nanostructured electrodes by different materials such as carbon-related materials, metal oxides Co_3O_4 , MnO_2 , Fe_2O_3 , ZnO , or carbon decorated ZnO [40,41].

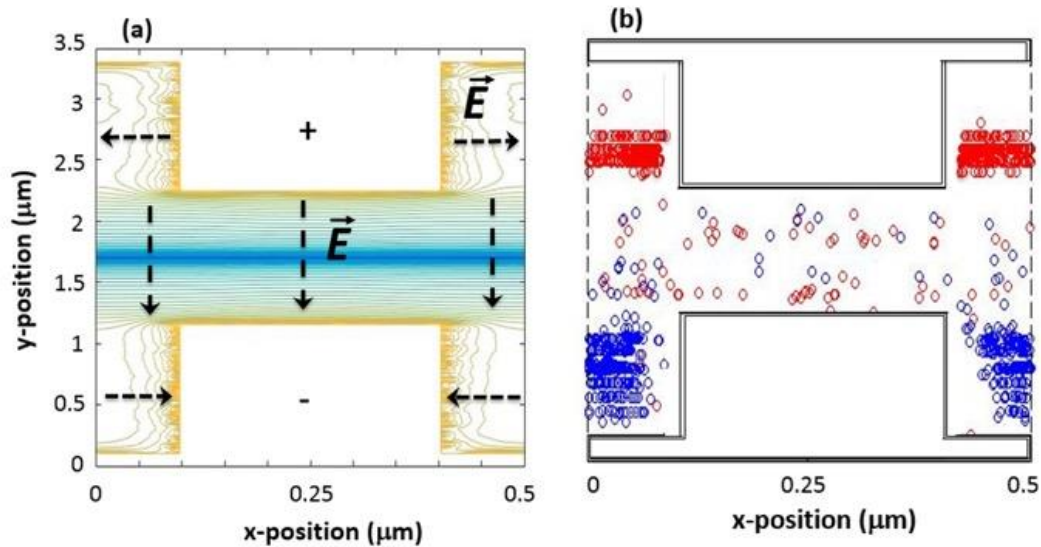


Figure 4.7. (a) Computed contours of the electric potential magnitude and the corresponding electric field in the CNU cell for configuration (1), with $W_S=0.2 \mu\text{m}=0.2LCNT$ and $DCNT=0.6$. (b) Time-evolution snapshot of electrolyte ionic distributions inside the same cell, where positive ions are indicated in blue and negative ions in red.

References

- [1] A. Orphanou, T. Yamada, C. Y. Yang, *Nanotechnology* **23**, 095401 (2012)
- [2] S. Pang, M. Anderson, T. Chapman, *J. Electrochem. Soc.* **147**, 444 (2000)
- [3] S. Gupta, M. Hughes, A. H. Windle, J. Robertson, *J. Appl. Phys.* **95**, 2038 (2004)
- [4] G. Zhou, D. Wang, F. Li, L. Zhang, Z. Weng, H. Cheng, *New Carbon Mater.* **26**, 180 (2011)
- [5] D. Tashima, M. Taniguchi, D. Fulikawa, T. Kijima, M. Otsubo, *Mater. Chem. Phys.* **115**, 69 (2009)
- [6] H. Wang, H. Dai, *Chem. Soc. Rev.* **7**, 2473 (2013)
- [7] E. Frackowiak, F. Beguin, *Carbon* **39**, 937 (2001)
- [8] R. Koetz, M. Carlen, *Electrochem. Acta* **45**, 2483 (2010)
- [9] A. Balducci, R. Dugas, P. L. Taberna, P. Simon, D. Plée, M. Mastragostino, S. Passerini, *J. Power Sources* **165**, 922 (2007)

- [10] E. Frackowiak, K. Jurewich, K. Szostak, S. Delpeux, F. Beguin, *Fuel Proc. Tech.* **77-78** 213 (2002)
- [11] M. Kaempgen, C. K. Chan, J. Ma, Y. Cui, G. Gruner, *Nano Lett.* **9**, 1872 (2009)
- [12] G. R. Li, Z. P. Feng, Y. N. Ou, D. Wu, R. Fu R, Y. X. Tong, *Langmuir* **26**, 2209 (2010)
- [13] K. Babe, K. Jurewicz, *Fuel Proc. Tech.* **77-78**, 181 (2002)
- [14] C. Liu, Z. Yu, D. Neff, A. Zhamu, B. Jang, *Nano Lett.* **10**, 4863 (2010)
- [15] T. Yamada, Y. Yamamoto, W. A. Harrison, *J. Vac. Sci. Technol. B* **14**, 1243 (1996)
- [16] T. Yamada, *J. Vac. Sci. Technol. B* **15**, 1019 (1997)
- [17] T. Yamada, C. W. Bauschlicher, H. Partridge, *Phys. Rev. B* **59**, 15430 (1999)
- [18] M. S. Dresselhaus, G. Dresselhaus, P. C. Eklund, *Science of Fullerenes and Carbon Nanotubes* (Academic, London, 1996)
- [19] T. Yamada, *Appl. Phys. Lett.* **76**, 628 (2000)
- [20] T. Yamada, *Appl. Phys. Lett.* **78**, 1739 (2001)
- [21] T. Yamada, *Appl. Phys. Lett.* **80**, 4027 (2002)
- [22] T. Yamada, T. Saito, M. Suzuki, P. Wilhite, X. Sun, N. Akhavantafiti, D. Fabris, C. Y. Yang, *J. Appl. Phys.* **107**, 044304 (2010)
- [23] Q. Cheng, T. Tang, J. Ma, H. Zhang, N. Shinya, L. Qin, *Phys. Chem. Chem. Phys.* **13**, 17615 (2011)
- [24] P. Kurzweil, M. Chwistek, *J. Power Sources* **176**, 2555 (2008)
- [25] E. Frackowiak, G. Lota, J. Pernak, *Appl. Phys. Lett.* **86**, 164104 (2005)
- [26] J. D. Stenger-Smith, C. K. Webber, N. Anderson, A. P. Chafin, K. Zong, J. R. Reynolds, *Electrochem. Soc.* **149**, A973 (2002)
- [27] H. Yamada, P. R. Bandaru, *Appl. Phys. Lett.* **104**, 213901 (2014)
- [28] H. Abruna, Y. Kiya, J. C. Henderson, *Phys. Today* **65**, 43 (2008)
- [29] R. Kötz, M. Carlen, *Electrochim. Acta* **45**, 2483 (2000)
- [30] H. J. In, S. Kumar, Y. Shao-Horn, G. Barbastathis, *Appl. Phys. Lett.* **88** 083104 (2006)
- [31] P. C. Chen, G. Shen, S. Sukcharoenchoke, C. W. Zhou, *Appl. Phys. Lett.* **94**, 043113 (2009)
- [32] J. Schindall, *IEEE Spectrum* **44**, 42 (2007)
- [33] T. Yamada, D. K. Ferry, *Phys. Rev. B* **47** 6416 (1993)
- [34] E. Frackowiak, K. Metenier, V. Bertagna, F. Beguin, *Appl. Phys. Lett.* **77**, 2421 (2000)
- [35] P. J. Price, "in *Fluctuation Phenomena in Solids*", edited by R. E. Burgess (Academic, New York, 1965), pp. 355-380
- [36] B. J. Alder and T. E. Wainright, *Phys. Rev. A* **1**, 18 (1970)
- [37] J. P. Hansen, D. Levesque, and J. J. Weis, *Phys. Rev. Lett.* **43**, 979 (1979)
- [38] C. Jacobini and L. Reggiani, *Rev. Mod. Phys.* **65**, 645 (1983)
- [39] J. Hardy, O. de Pazzis, and Y. Pomeau, *Phys. Rev. A* **13**, 1949 (1976)
- [40] X. Zhao, B. Chu, B. Ballesteros, W. Wang, C. Johnston, J. Sykes, P. Grany, *Nanotechnology* **20**, 065605 (2009)
- [41] X. Jian, G. Chen, C. Wang, L. Yin, G. Li, P. Yang, L. Chen, X. Bao, Y. Gao, Y. Feng, *Nanotechnology* **26**, 125705 (2015)
- [42] R. Signorelli, D. C. Ku, J. G. Kassakian, J. E. Schindall, *Proc. IEEE* **97**, 1837 (2006)
- [43] J. H. Kim, K. W. Nam, S. B. Ma, K. B. Kim, *Carbon* **44**, 1963 (2006)
- [44] R. Shah, X. Zhang, and S. Talapatra, *Nanotechnology*, **20**, 395202 (2009)
- [45] J. Y. Lee, K. Liang, K. H. An, Y. H. Lee, *Synthetic Metals*, **150**, 153 (2005)

- [46] C. Portet, P. L. Taberna, P. Simon, E. Flahaut, C. Laberty-Robert, *Electrochimica Acta* **50**, 4174 (2005)
- [47] H. Abruna, Y. Kiya, J. C. Henderson, *Phys. Today* **65**, 43 (2008)
- [48] C. Meng, C. Liu, L. Chen, C. Hu, S. Fan, *Nano Lett.* **10**, 4025 (2010)
- [49] K. Hyeok, W. S. Kim, Y. S. Park, J. M. Moon, D. J. Bae, S. C. Lim, Y. S. Lee, Y. H. Lee, *Adv. Funct. Mater.* **11**, 387 (2001)
- [50] K. Hyeok, K. K. Jeon, J. K. Heo, C. Lim, D. J. Bae, Y. H. Lee, *J. Electrochem. Soc.* **149**, A1058 (2002)
- [51] T. Yamada, D. K. Ferry, *Phys. Rev. B* **48**, 8076 (1993)

CHAPTER 5

Conclusions and Future Work

We have proposed to create a physical model for a UC using CNT arrays as electrodes. The performance of the modeled UC is analyzed based on solutions of Poisson's equation obtained using molecular dynamic techniques. Although the designed algorithm for the analysis and correlation with experiment are for a CNU, our methodology is well suited for other electrode materials such as carbon-related materials, metal oxides Co_3O_4 , MnO_2 , Fe_2O_3 , ZnO , or carbon decorated ZnO . Using such algorithm to develop the necessary computational scheme will allow us to use our model to understand how the UC performance is related to certain UC geometrical and electrolyte features. So far optimizing the UC features has been largely dependent on empirical data and trial-and-error experimentation. We have used our model and computational methodology to perform a UC optimization analysis and examine features such as CNT diameter, length, and density. This analysis will elucidate how these variables affect the UC performance, and lead to the eventual optimization of the CNU cell.

The proposed methodology consists of two distinct steps. First, the equipotential electrode charge distribution is determined using full molecular dynamics techniques, that is, the charges in the electrodes are given enough time to interact and reach steady state allowing full electrode-to-electrode ion interaction. Second, once the electrode equipotential is achieved, the electrolyte is allowed to interact with the positive and negative electrodes, and the current through the capacitor is computed. With the voltage defined as an input in the simulation and from the current obtained from the electrolyte distribution and their respective electrode

interactions, the complex impedance of the CNU is computed and compared with existing experimental data. The capacitance and resistance extracted from the simulation results compare well with their experimental counterparts [1] and our results have been reported [2].

Further, we have applied our MD technique to perform a CNU optimization for the purpose of a cell design. We have investigated the effects of electrode-to-electrode separation, CNT length, and CNT density on the electrical performance of the CNU cell, using a particle-based model. Assuming a metallic and equipotential electrode surface and solving for the electric field in the device using molecular dynamics, we have simulated the electrolyte ionic motion and spatial distributions, computed the capacitor current, and hence determined all electrical parameters. Our results compare well with existing experimental data. In addition, the computed capacitance has an optimal range of CNT linear packing density D_{CNT} values, beyond which the performance degrades dramatically, even dropping below the equivalent parallel-plate capacitance, at which $L_{CNT} = 0$ in the capacitor cell. In particular, we have shown that the linear capacitance density CD_L increases with increasing D_{CNT} up to the point where the CNT-to-CNT separation W_s reaches $\sim 2L_{CNT}/3$ before dropping sharply. Such dramatic decrease in CD_L is attributed to the occurrence of electrolyte ionic traps between adjacent CNTs at close proximity. This finding is supported by computed potential contours and electric field, as well as ionic distributions at two different values of D_{CNT} . It is also consistent with reported experimental data. The approach and the results presented here can lead to a versatile UC model development and definition of guidelines for CNU cell design for eventual implementation.

Our methodology is the first that uses a particle-based ultracapacitor model, based partly on molecular dynamic techniques that we have developed, tested, and correlated to existing

experimental data. Our methodology can be used to extract the electrical characteristics of an ultracapacitor of any electrode shape or any metallic electrode material. In our research we have used our developed molecular dynamics algorithm systematically to firstly extract, correlate and understand the Nyquist and Cyclic- Voltametry plots of an ultracapacitor as well as to understand how various geometrical features can affect the electrical performance of a vertically grown CNT capacitor. Such features are the CNT density, the CNT length and the electrode to electrode separation. Further, our particle based model can predict an optimal CNT density range over which the capacitance density of the “device” drops dramatically due to the formation of ionic traps in the high CNT regime. Our approach can allow a systematic ultracapacitor design and optimization allowing for electrode shape variations, electrode material variations and electrolyte type changes. Our simulation results agree well with current experimental data and theoretical predictions, and have been reported [3].

Our research is still in its beginning phase. What we have achieved thus far is to prove that molecular dynamics through pure ionic movement and distributions in the system can fully characterize the electrical performance of an ultracapacitor. In addition to the geometrical features above relating the CNU performance to its key geometrical parameters, we would also like to examine the effect of the electrolyte ionic mass and volume density on the CNU performance. Although extensive experimental work is being conducted in understanding how the electrolyte type (aqueous, non aqueous, ionic, gel-polymer, polymer, organic, e.t.c.) can affect the overall capacitance density of a carbon based material electrode supercapacitor, [4-14], there is no systematic science base approach to quantify the electrolyte performance in the ultra capacitor. The proposed methodology will be employed to analyze the effect of the

electrolyte dynamics on the UC AC performance, from which we can better understand how the density, mass and charge of the electrolyte can affect the double-layer capacitance, resistance, and inductance.

Further, we would like to eventually extend this algorithm to a full 3D computational model. Although our geometry transformation from a 3D to a 2.5D problem has proven to be rather accurate [2,12, 13], we want to extend this problem to a fully 3D structure, always based on molecular dynamics techniques [16-20]. Our 2.5D transformation of the problem can successfully recover all the first order effects of the problem, it ignores second order effects of the electrode such as mesopores and roughness [21-24] along the CNTs' electrode surface. Mesopores and roughness are in general geometrical "imperfections" that can accumulate extra charge along the electrode structure and affect the double layer capacitance and the total capacitance density on second order. Determine the dependence of the CNU capacitance density on these second order imperfections would further improve the accuracy of our model.

In addition to improving the accuracy model to a second order using a full 3D molecular dynamics algorithm, we would also like to proceed with a cell fabrication and build a CNT capacitor for lab characterization and correlation to our computational model. Figure 5.1 shows the schematic of a 3D model. Compared to the 2.5D model that we have developed in chapter-2 (Figure 2.1), the 3D equivalent computational cell will be more scalable to a real experimental.

We have shown that our research has produce the much-needed results that are consistent with existing experimental data and can lead to a comprehensive understanding of the CNU operation and eventual cell design using a systematic approach.

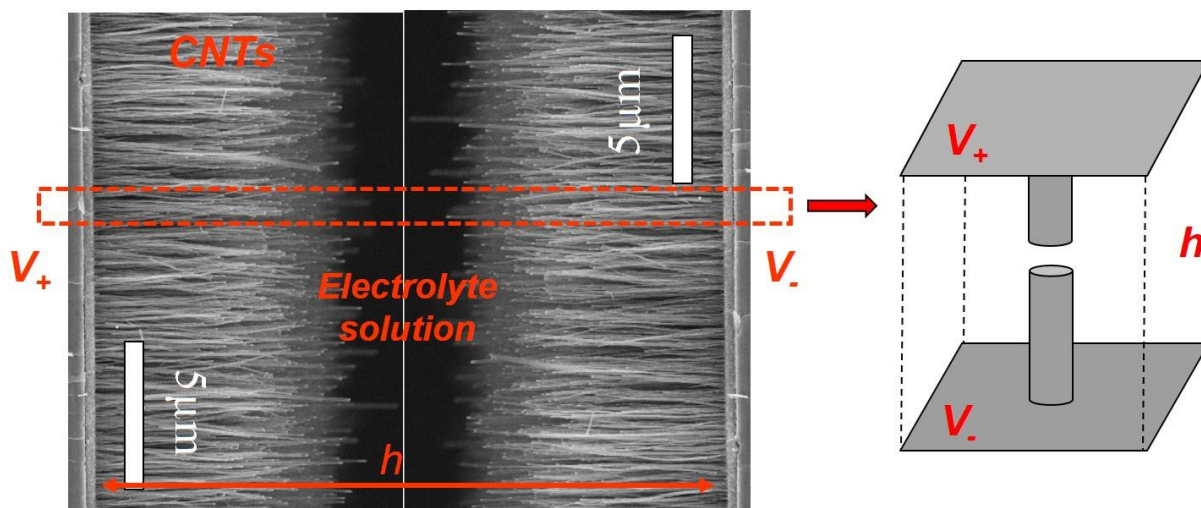


Figure 5.1. A graphical illustration of a CNT ultra capacitor cell on the left and the equivalent 3D unit cell depicted on the right. The cell will consist of a single CNT on each one of the anode and cathode electrodes.

References

- [1] E. Frackowiak, K. Metenier, V. Bertagna, F. Beguin, *Appl. Phys. Lett.* **77**, 2421 (2000)
- [2] A. Orphanou, T. Yamada, C. Y. Yang, *Nanotechnology* **23**, 095401 (2012)
- [3] A. Orphanou, T. Yamada, C. Y. Yang, *J. Appl. Phys.*, **119**, 214311 (2016)
- [4] J. N. Barisci, G. G. Wallace, D. R. MacFarlane, and R. H. Baughman, *Electrochemistry Elecom* **6**, **22** (2004)
- [5] Y. J. Kang, H. Chung, C. H. Han, W. Kim, *Nanotechnology* **23**, 6 (2012)
- [6] Y. J. Kang, H. Chung, W. Kim, *Synthetic Metals* **166**, 40 (2013)
- [7] Y. Zhang, X. Sun, L. Pan, H. Li, Z. Sun, C. Sun, B. K. Tay, *Alloys Compd.* **480**, L17 (2009)
- [8] B. Kim, H. C, and W. Kin, *Nanotechnology*, **23**, 15 (2012)
- [9] V. Khomeiko, E. Reymundo-Pinero, E. Frackowiak, F. Beguin, *Applied Physics A* **82.4**, 567 2006
- [10] C. Ported, P. L. Taberna, P. Simon, E. Flahaut, *Journal of power sources* **139.1**, 371 (2005)
- [11] M. D. Stoller, R. S. Ruoff, *Energy & Environmental science* **3.9**, 1294 (2010)
- [12] C. Qian, J. Tang, J. Ma, H. Zhang, N. Shinya, L. C. Qin, *Physical Chemistry Chemical Physics* **13.39**, 17615 (2011)
- [13] Y. Chen, X. Zhang, D. Zhang, P. Yu, Y. Ma, *Carbon*, **49.2**, 573 (2011)
- [14] J. Huang, B. G. Sumpter, V. Meunier, *Chemistry-A European Journal* **14**, 22 (2008)
- [15] T. Yamada, Ferry D K 1993 *Phys. Rev. B* **47** 6416
- [16] P. J. Price, "in *Fluctuation Phenomena in Solids*", edited by R. E. Burgess (Academic, New York, 1965), pp. 355-380
- [17] B. J. Alder, T. E. Wainright, *Phys. Rev. A* **1**, 18 (1970)
- [18] J. P. Hansen, D. Levesque, J. J. Weis, *Phys. Rev. Lett.* **43**, 979 (1979)
- [19] C. Jacobini, L. Reggiani, *Rev. Mod. Phys.* **65**, 645 (1983)

- [20] J. Hardy, O. de Pazzis, and Y. Pomeau, *Phys. Rev. A* **13**, 1949 (1976)
- [21] Y. Zhu, et al. *Science* **332**, 1537 (2011)
- [22] M. Liang, B. Luo, L. Zhi, *Int. J. Energy* **33**, 1161 (2009)
- [23] L. Kun, et al. *Journal of Materials Chemistry A*, **1/34**, 9730 (2013)
- [24] Z. Jing et al. *Electrochimica Acta* **104**, 110 (2013)

Appendix A

Computational Algorithm Flow Diagrams

In this section we present the fundamental flow of the total current computation in the simulated capacitor unit cell. As we have already mentioned, the process of extracting the current in the capacitor volume is a two-step process.

Firstly, we run a full Molecular Dynamics simulation [1-6] which couples the electric forces between the anode and cathode ions respectively. During this simulation we allow the anode and cathode charges to fully interact as a coupled system to allow the development of an equipotential anode and cathode surfaces. This is consistent with a fully metallic electrode. Once in their final equipotential position, the anode and cathode ions are then frozen in position and scaled accordingly in order to obtain the desired electrode voltage magnitude.

With the equipotential anode and cathode electrodes achieved, we proceed on to the second part of the computation. The electrolyte ions are now allowed to interact with the anode and cathode charges [1-13] according to the the electrode applied voltage. This interaction will result in convection and displacement currents in the capacitor volume. Given the applied voltage potential source on the electrodes and the resulting current, we then proceed to calculate the impedance of the computational cell. With the voltage defined, the computed current and the calculated impedance, the electrical performance of the computational capacitor cell is then fully described.

Let us start with an in-depth description of the first part of the computation which is the development of the equipotential anode and cathode metallic electrode surfaces using a full Molecular Dynamics algorithm. The flow-chart below, Figure A.1, illustrates the computational process in a more detail:

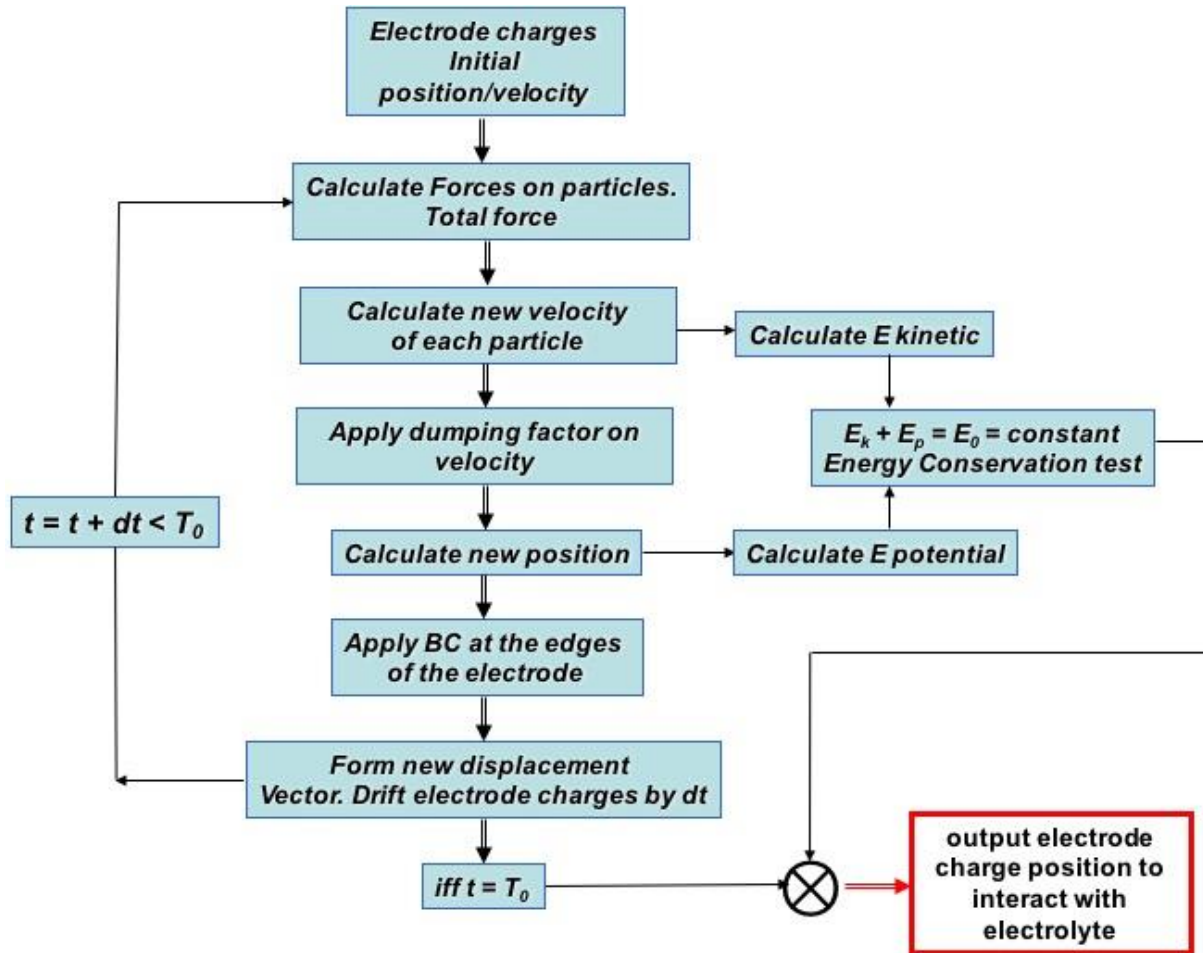


Figure A.1. Step 1 of 2 of the CNU impedance computational and extraction process. An electrode Molecular Dynamics technique is implemented to calculate the electrode equipotential and metallic interface between the electrode ions and the electrolyte in the capacitor volume.

First, we randomly position the anode and cathode ions in their respective electrode volume and give them an initial velocity. We then proceed to calculate all the cumulative total

force on each one of the anode and cathode ion charges and with this known, we can now calculate the new velocity of each one of the electrode charges. Once the calculated new velocity is known, we apply the velocity dumping factor and calculate the electrode ion new position.

Here we need to stress the importance of the velocity dumping factor. In the absence of this resistive force in the anode and cathode electrodes, the electrode charges would indefinitely oscillate in the electrode volume resulting in a non-convergent time simulation. This would result in a non-metallic electrode surface with loss of equipotential along the electrode boundaries. The challenge in this step is to define the proper resistance for the electrode charges so that the energy is smoothly conserved throughout the time-iteration process. If the energy is not smoothly conserved throughout the full length of the time iteration, then the simulation needs to be restarted. The time step in this time-iterative process is also a very critical parameter in achieving the proper conservation of energy. Too large of a time step and the simulation is non convergent, too small and the simulation is extremely lengthy requiring huge amount of computational resources. The conservation of energy check at this stage is a crucial step in dictating the proper deceleration of the electrode charges and the proper electrode charge distribution along the electrode boundary to achieve the desired metallic behavior. Without the proper equipotential metallic electrode boundaries, the current calculation in the second part of the simulation is neither stable nor convergent.

Once the new ion position is calculated then we the electrode boundary conditions. As we have described in section 2, the electrode edges are nothing but perfect reflectors which conserve the kinetic energy and momentum of the bouncing ions. Once the boundary condition is applied, the new displacement vector is formed, the time is incremented and the time iteration

continues until the anode and cathode charges are well situated in an equipotential along the electrode surfaces. When this condition is met, the electrode has the proper and required metallic form. The electrode charges are now frozen in place and their position becomes available for the next part of the computational process which is the calculation of total current in the capacitor volume.

The flow-chart below, Figure A.2, illustrates the computational flow of the capacitor current in a proper detail:

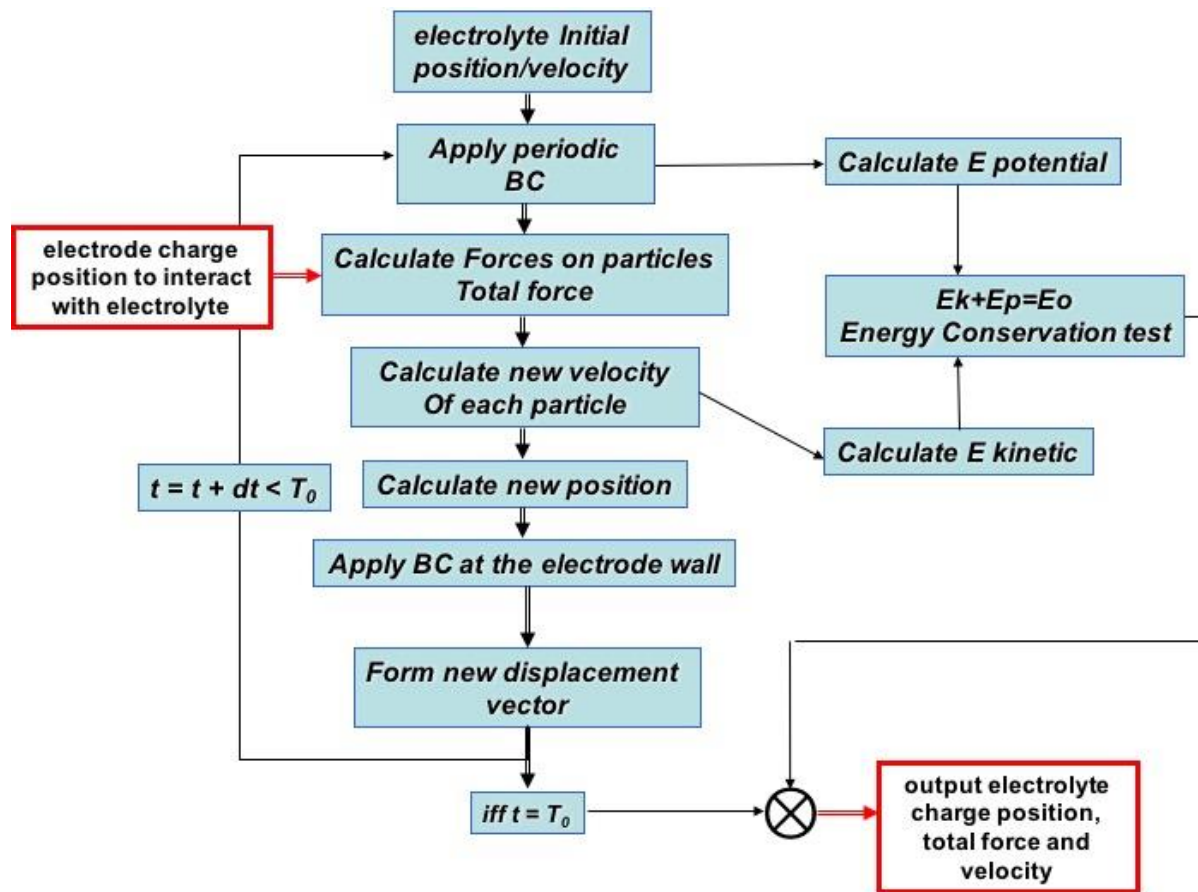


Figure A.2. Step 2 of 2 of the CNU impedance computational and extraction process. Electrolyte partial Molecular Dynamics technique is implemented to calculate the electrode to the electrolyte interaction in the capacitor volume. This step requires the input from step 1 as described in Figure A1.1 to calculate the total convection and displacement currents in the capacitor volume.

In this part of the computation, we firstly randomly position the electrolyte ions in the capacitor volume. An initial velocity could be applied at this stage to help distribute the electrolyte as dictated by the electrode physics quicker in time, yielding a more stable simulation and a longer time span of meaningful convergent data. Once this is achieved then we proceed on to apply the electrolyte boundary conditions as dictated by the capacitor computational unit cell boundaries. On the north and south of the computation unit cell we have the anode and cathode electrodes that are modeled as perfect bouncing walls. In addition, on the east/west edges of the computational unit cell we have applied periodic boundary conditions, as described in detail in section 2. The periodic boundary condition was the most appropriate boundary for this purpose because it could mimic the interaction of adjacent CNTs in the CNU, while conserving at the same time the kinetic energy and momentum of the system.

At the next step of the computation, we calculate the total force on the electrolyte particles. This is the stage where the algorithm will take in as an input from the first part of the simulation the electrode charges spatial information and allow the them to electrically interact with the electrolyte. The total force on each one of the electrolyte ions is hence calculated. With the total force now defined, we calculate the velocity and hence the new electrolyte displacement in the time-step defined by the user. Figure A.3 below illustrates the computed ensample average total force and the ensample average force on the positively and negative electrolyte ions, respectively. The displacement current is proportional to the derivative of the ensample average force. A displacement current computation example is illustrated in figure A.4 and is computed as the derivative of the ensample average total force of the electrolyte.

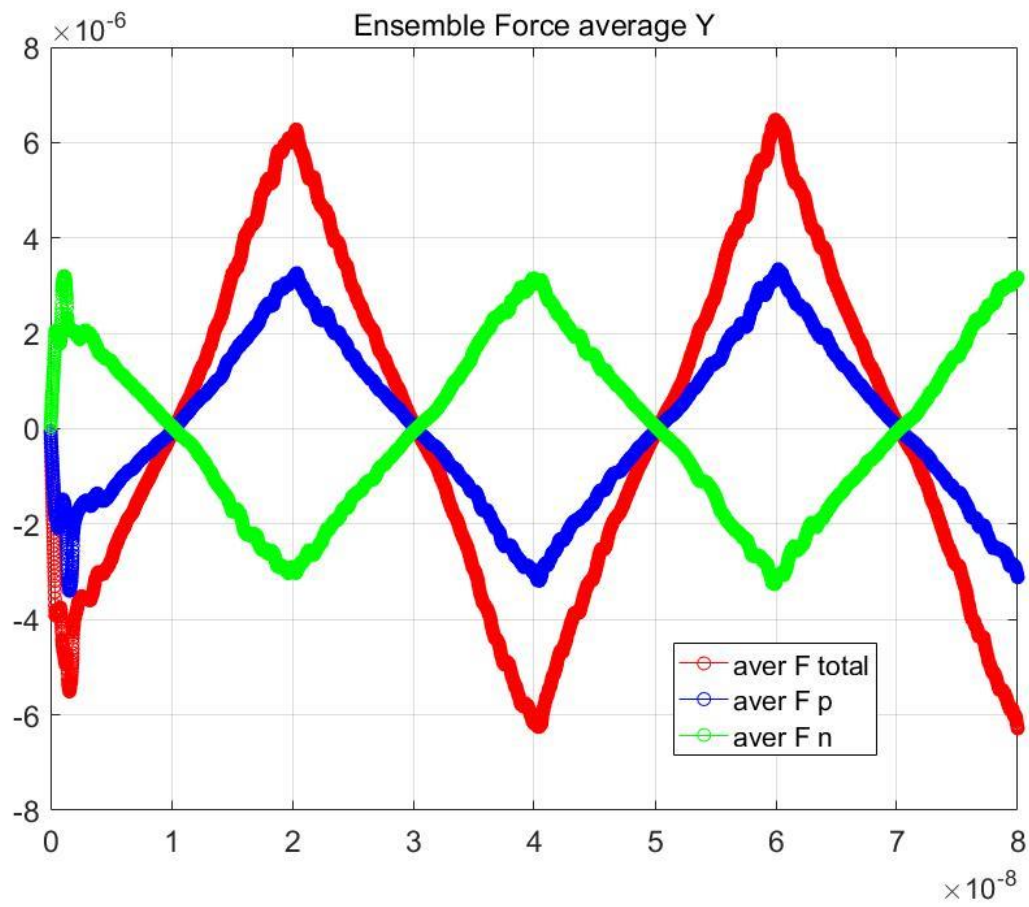


Figure A.3. The ensemble average total force and the ensemble average force on the positive and negative electrolyte ions, respectively.

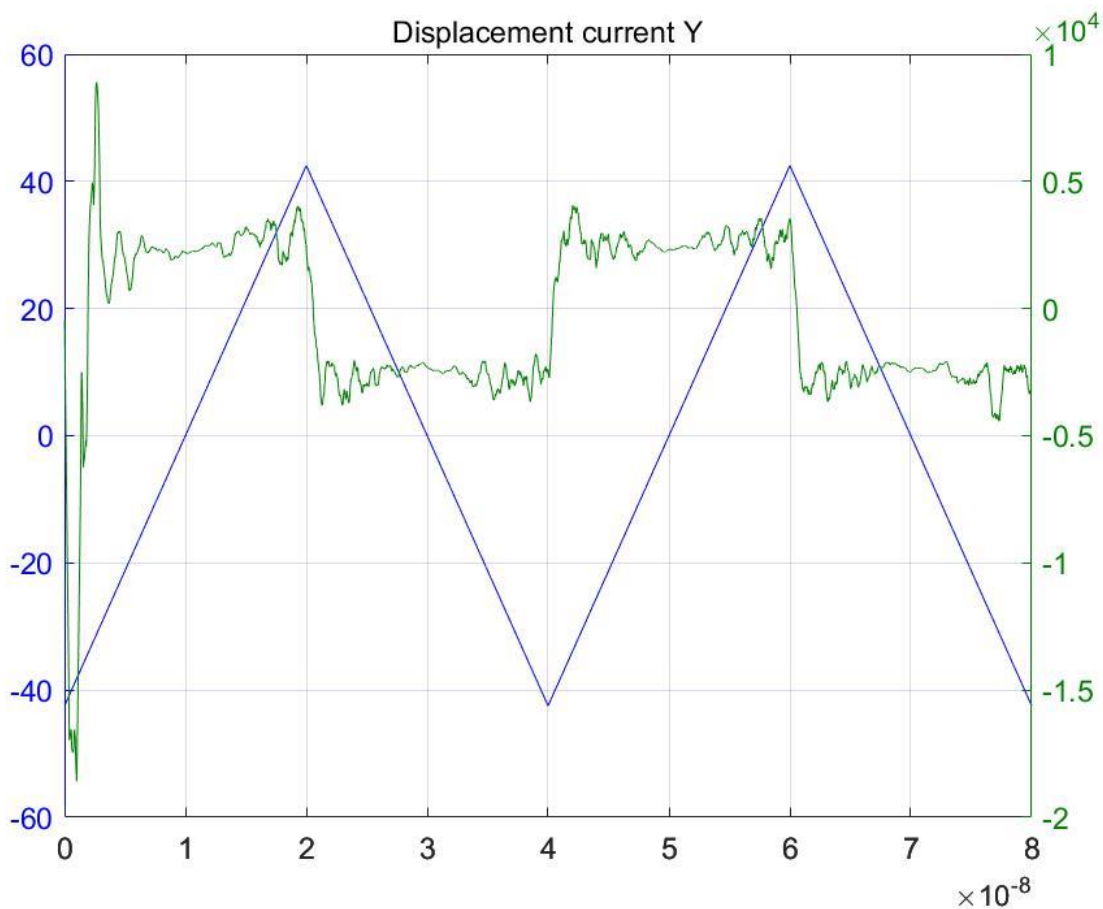


Figure A.4. Illustration of the calculation of the displacement current in the capacitor volume as a function of the capacitor electrode ramp voltage. The displacement current is calculated from the derivative of the ensemble average total electrolyte electromotive force.

We proceed on to apply the boundary conditions on the electrode wall, form a new displacement vector for the electrolyte ions, increase the time by a single time step and proceed on with the iteration until both the conservation of energy and total time is achieved. Similar to the first part of the simulation (the electrode Molecular Dynamics), the electrolyte dynamics algorithm conserves the total energy in the system on every time step and at the end of the computation it outputs the electrolyte drift velocity, total force and position as a function of time.

Once the electrolyte velocity of every electrolyte particle is calculated, the velocity ensemble average over all the electrolyte charges is calculated. This enables us to calculate the ensemble average drift current in the capacitor volume. The drift current is hence LMS fitted into a sinusoid for the calculation of the Nyquist plot as described in chapter 3.1 With the electrode voltage defined and the ensemble average current calculated, we can compute the impedance of the capacitor. In addition, knowing the ensemble average force on the electrolyte particles, we can calculate the total displacement current in the capacitor for the extraction of the CV plot as described in chapter 3.2.

Figure A.5 below illustrates the ensemble of all the electrolyte positive and negative ion currents, the ensemble average total current and the LMS fitted current used in the computation of the capacitor impedance. It is meant to visualize the calculation of the convection current density in the capacitor volume.

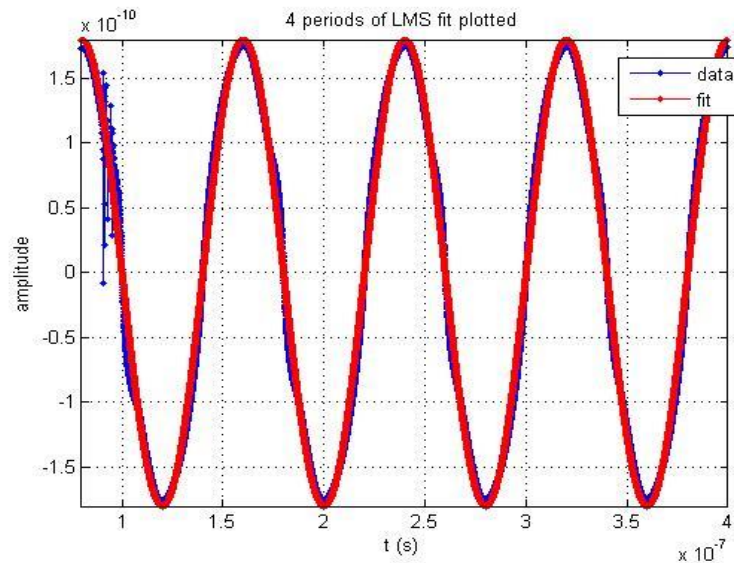


Figure A.5. Illustration of the convection current calculation in the capacitor volume. The average ensemble current density (shown in blue markers) computed in our simulation is LMS fitted to a sinusoid waveform (red markers) for the extraction of the average phase and amplitude of the capacitor impedance response to a sinusoidal electrode input voltage.

References

- [1] T. Yamada and D. K. Ferry *Phys. Rev. B* **47**, 6416 (1993)
- [2] A. K. Rappa, W. A. Goddard III *J. Phys. Chem.* **95**, 8 (1991)
- [3] B. Ensing, S. O. Nielsen, P. B. Moore, M. L. Klein, M. Parrinello *J. Chem Theory Comput.* **3** (3), 1100 (2007)
- [4] K. Leung, J. L. Budzien *J. Phys. Chem* **12**, 6583 (2010)
- [5] K. Tasaki, K. Kanda, S. Nakamura, M. Ue *J. Electrochem Soc.* **150**, A1628 (2003)
- [6] P. G. Wolynes *Ann. Rev Phys. Chem.* **31**, 345 (1980)
- [7] P. B. Balbuena, K. P. Johnson, P. J. Rossky *J. Phys. Chem.* **100**(7), 2706 (1996)
- [8] P. S. Crozier, R. L. Rowley, D. Henderson, *J. Chem. Phys.* **113**, 9202 (2000)
- [9] S. Chowdhuri, A. Chandra *J. Chem. Phys.* **115**, 3732 (2001)
- [10] A. Geiger *Berichte der Bunsengesellschaft für physikalische Chemie* **85**, 52 (1981)
- [11] S. T. Cui, H. D. Cochran *J. Chem Phys.* **117**, 5850 (2002)
- [12] I. C. Bourg, G. Sposito *J. Colloid and Int. Sci.* **360**, 701 (2011)
- [13] J. Vatamanu, O. Borodin, G. D. Smith *J. Phys. Chem. C* **2012**, 116 (2011)

Publications of Antonis A. Orphanou

Refereed Journals

- **A. Orphanou**, T. Yamada, and C.Y. Yang, "Optimization of carbon nanotube ultracapacitor for cell design," *Journal of Applied Physics* 119, 214311 (6 pp) (2016).
- **A. Orphanou**, T. Yamada, and C.Y. Yang, "Modeling of a carbon nanotube ultracapacitor," *Nanotechnology* 23, 095401 (7 pp) (2012).

Conference Presentations

- Ryan Coutts, **Antonis Orphanou**, and Manuel Luschas, "Correlation Methodology for Generating IBIS-AMI Models for Multi-Gigabit SerDes Devices," *DesignCon 2012*, Santa Clara CA, January 31-February 2, 2012.
- **A. Orphanou**, T. Yamada, and C.Y. Yang, "Modeling of Nanocarbon Ultracapacitor," Materials Research Society Spring Meeting, Symposium **M**: Nanostructured Materials for Energy Storage, San Francisco, April 25-29, 2011.
- Ryan Coutts and **Antonis Orphanou**, "AMI Modeling Methodology and Measurement Correlation of a 6.25Gb/s Link," IBIS Summit, San Diego CA, June 5, 2011.
- **A. Orphanou**, T. Yamada, and C. Y. Yang, "Modeling carbon nanotube ultracapacitor," IEEE Nanotechnology Materials and Devices Conference 2010 (NMDC 2010), Monterey, CA, October 12-15, 2010.
- **A. Orphanou**, T. Yamada, and C. Y. Yang, "Modeling carbon nanotube ultracapacitor," International Conference on Materials for Energy, Karlsruhe, Germany, July 4-8, 2010.
- Jose Luis Pino, Amolak Badesha, **Antonis Orphanou**, Manuel Luschas, and Halil Cirit, "Automated AMI modeling and correlation," IBIS Summit, Anaheim CA, June 15, 2010.
- **A. Orphanou**, T. Yamada, and C.Y. Yang, "Science-based modeling of carbon nanotube ultracapacitor," 38th Annual Electronic Materials Symposium, Santa Clara, April 16, 2010.
- **A. Orphanou**, T. Yamada, and C.Y. Yang, "Modeling of 3-D Energy Storage in Carbon Nanotube Ultracapacitor," Materials Research Society Spring Meeting, Symposium Y: Computational Approaches to Materials for Energy, San Francisco, April 5-9, 2010.
- **A. Orphanou**, T. Yamada, and C.Y. Yang, "Modeling of 3-D energy storage in carbon nanotube ultracapacitor," Materials Research Society Spring Meeting, Symposium P: Three-dimensional Architecture for Energy Generation and Storage, San Francisco, April 13-17, 2009.